ARTICLE

A tensile trilayered cytoskeletal endotube drives capillary-like lumenogenesis

Liakot A. Khan[1], Gholamali Jafari[1], Nan Zhang[1,2], Edward Membreno[1], Siyang Yan[1], Hongjie Zhang[1,3], and Verena Gobel[1]

Unicellular tubes are components of internal organs and capillaries. It is unclear how they meet the architectural challenge to extend a centered intracellular lumen of uniform diameter. In an RNAi-based *Caenorhabditis elegans* screen, we identified three intermediate filaments (IFs)—IFA-4, IFB-1, and IFC-2—as interactors of the lumenal membrane-actin linker ERM-1 in excretory-canal tubulogenesis. We find that IFs, generally thought to affect morphogenesis indirectly by maintaining tissue integrity, directly promote lumenogenesis in this capillary-like single-cell tube. We show that ERM-1, ACT-5/actin, and TBB-2/ tubulin recruit membrane-forming endosomal and flux-promoting canalicular vesicles to the lumen, whereas IFs, themselves recruited to the lumen by ERM-1 and TBB-2, restrain lateral vesicle access. IFs thereby prevent cystogenesis, equilibrate the lumen diameter, and promote lumen forward extension. Genetic and imaging analyses suggest that IFB-1/IFA-4 and IFB-1/IFC-2 polymers form a perilumenal triple IF lattice, sandwiched between actin and helical tubulin. Our findings characterize a novel mechanism of capillary-like lumenogenesis, where a tensile trilayered cytoskeletal endotube transforms concentric into directional growth.

Introduction

All internal organs and the vasculature are built of tubes. Tubes are polarized epithelia or endothelia with distinctive lumenal surfaces, constructed for horizontal transport and vertical exchange of liquids, solids, and gases. Defects in tube development and maintenance cause congenital organ and vascular malformations and internal organ dysfunction and vessel disease (Hogan and Kolodziej, 2002; Carmeliet, 2003). Although complex, the process of tube and lumen morphogenesis only uses a limited number of blueprints, phylogenetically conserved to the molecular level (Lubarsky and Krasnow, 2003). Most biological tubes are built from multiple cells, but some are built from single cells. Multicellular tubes form lumens between cells (intercellular), secured by junctions; unicellular tubes form lumens inside a cell (intracellular) by cell wrapping or cell hollowing, generating tubes with or without junctions (seamless tubes), respectively. Unicellular seamless tubes constitute up to half of human capillary beds and are conserved from plants to humans (Bär et al., 1984; Sundaram and Cohen, 2017).

The molecular, cellular, and biophysical mechanisms of intracellular lumen extension in capillary-like unicellular seamless tubes are poorly understood. Current hypotheses include: (1) central vacuole coalescence, (2) endomembrane extension from an adjacent junction, and (3) invagination of the neighboring cell membrane (Folkman and Haudenschild, 1980; Kamei et al., 2006; Gervais and Casanova, 2010; Herwig et al., 2011; Sigurbjörnsdóttir et al., 2014). All hypotheses implicate vesicular trafficking in intracellular lumenogenesis, but how it affects this process remains unclear. Among cytoskeletal elements, actin microfilaments (AFs) were proposed to provide mechanical support for intracellular lumenal membrane expansion and microtubules (MTs) to deliver vesicles to the lumen (Schottenfeld-Roames and Ghabrial, 2012). Cytoplasmic intermediate filaments (cIFs), based on their resilient properties, are thought to maintain inter- and intracellular lumen integrity (Carberry et al., 2012; Kolotuev et al., 2013; Al-Hashimi et al., 2018). The biophysical contribution of flux to lumenogenesis was demonstrated in zebrafish vasculogenesis and *Caenorhabditis elegans* excretory canal morphogenesis (Khan et al., 2013; Kochhan et al., 2013; Gebala et al., 2016). Both molecular and architectural mechanisms of unicellular tubulogenesis are conserved; homologues of human vascular disease genes (e.g., the cerebral cavernous malformation gene) also cause tubulogenesis defects in *Drosophila melanogaster* and *C. elegans* (Song et al., 2013; Lant et al., 2015).

[1]Mucosal Immunology and Biology Research Center, Developmental Biology and Genetics Core, Massachusetts General Hospital for Children, Harvard Medical School, Boston, MA; [2]Key Laboratory of Zoonosis Research, Institute of Zoonosis, College of Veterinary Medicine, Jilin University, Changchun, China; [3]Faculty of Health Sciences, University of Macau, Taipa, Macau, China.

Correspondence to Verena Gobel: vgobel@mgh.harvard.edu.

The five-cell *C. elegans* excretory system functions in osmoregulation and waste excretion (Nelson and Riddle, 1984; Sundaram and Buechner, 2016). Its single canal cell, connected to the excretory duct by its only junction, expands its size 2,000 times to build four canals. The correspondingly dramatic extension of its apical membrane constitutes the process of intracellular lumenogenesis (Fig. 1, a and b). Two distinct endomembrane systems, endosomal vesicles and inter- and lumen-connected canalicular tubulovesicles, were proposed to provide lumenal membrane and translumenal flux, respectively, for the formation and function of this lumenal endotube (Fig. 1 c; Khan et al., 2013; Kolotuev et al., 2013). This junction-less tube system is thus a unique model to investigate polarized endo- and plasma membrane biogenesis, intracellular lumenogenesis, and seamless tubulogenesis in vivo.

We previously showed that the conserved apical/lumenal membrane-actin linker ERM-1/ezrin-radixin-moesin is strictly required for *C. elegans* excretory canal lumenogenesis (Khan et al., 2013). ERM-1 recruits actin to the lumen and promotes lumenal membrane expansion and translumenal flux. Here, we broaden the analysis of intracellular lumenogenesis to actin/AFs and extend it to intermediate filaments (IFs) and tubulin/MTs. We find that perilumenal ACT-5/actin is indispensable for lumen formation, whereas three perilumenal cIFs (IFA-4, IFB-1, and IFC-2) and TBB-2/tubulin drive the lumen's forward extension. The three cytoskeletal filamentous structures cooperate in lumen extension via distinct roles at the vesicle–lumen interface.

Results

Forward screens identify IFA-4, IFB-1, and IFC-2 as nonredundant ERM-1 interactors in intracellular lumenogenesis

The *C. elegans* excretory canal cell directs two canals each toward the nose and tail (Fig. 1 a). Anterior and posterior canal extension (forward extension) proceeds from lateral canal bifurcations through late embryogenesis and four larval stages (L1–L4), catching up with body length at the L2 stage (Fig. 3 e; Buechner, 2002). Intracellular lumen extension follows canal extension with delay. To distinguish the ultrathin lumenal endotube from the surrounding canal tube by confocal microscopy, the apical/lumenal membrane must be marked (Fig. 1 b and Materials and methods). Overexpression of the lumenal membrane–actin linker ERM-1 (ERM-1^{++}) generates small lumenal cysts, a thickened lumenal actin coat, and shortened lumens and canals (Fig. 1, h and i). To investigate ERM-1–dependent intracellular lumenogenesis, we performed a visual RNAi modifier screen of ERM-1^{++} P$_{sulp-5}$::GFP-labeled canals (Khan et al., 2013). Among 26 strong loss-of-function enhancers, three were found to be cIF genes. ERM-1^{++} *ifa-4-, ifb-1-,* and *ifc-2(RNAi)* animals each lacked all forward canal extension and instead developed cystic structures at canal bifurcations (Fig. 1, f and j; and Fig. S1, a–c). Depending on their intralumenal or cytoplasmic location, cystic canal structures can represent different phenotypes, here distinguished as cysts versus vacuoles, respectively. ERM-1^{++} *ifa-4-, ifb-1-,* and *ifc-2(RNAi)* cystic structures were identified as

intralumenal cysts by labeling with the apical/lumenal membrane component ACT-5::GFP (Fig. S1 k; Khan et al., 2013). We conclude that loss of three cIFs directly enhances ERM-1^{++} lumenal defects.

The *C. elegans* genome contains 11 cIFs (Karabinos et al., 2001). To comprehensively examine cIF function in ERM-1–dependent intracellular lumenogenesis, each of the 11 cIFs was knocked down in ERM-1^{++} animals whose canal cytoplasm was labeled with P$_{sulp-5}$::GFP. No additional cIFs modified the ERM-1^{++} canal phenotype, although IFC-1 depletion mildly enhanced the phenotype (Fig. 1 k). These results reveal a nonredundant interaction of IFA-4, IFB-1, and IFC-2, and possibly IFC-1, with ERM-1 in intracellular lumen and single-cell canal morphogenesis.

cIFs have been proposed to maintain the structure of *C. elegans* excretory canals (Khan et al., 2013; Kolotuev et al., 2013; Al-Hashimi et al., 2018). To investigate whether and how cIFs maintain canal structure, we first comprehensively assessed the effect of all *C. elegans* cIFs on the morphogenesis of P$_{sulp-5}$::GFP-labeled WT canals. RNAi with *ifa-4, ifb-1,* and *ifc-2* RNAi, but not any of the other eight cIFs, resulted in short canals with cystic structures, consistent with a specific and separable canal function of the three ERM-1–interacting cIFs (Fig. 1, l–p). ERM-1::GFP or ACT-5::GFP labeling identified the structures as intralumenal cysts and determined that lumens were truncated inside the shortened canals (Fig. S1, h–k). *ifb-1* RNAi was the most severe, copying the cIF-loss enhanced ERM-1^{++} phenotype (large, cell-body close cysts, with almost no canal/lumen extension; Fig. 1, f, j, and n). *ifa-4* and *ifc-2* RNAi caused smaller cysts along longer canals, generating a meandering lumen with a grapes-on-a-vine multicyst pattern, merging to larger cysts over time (Fig. 1, g, m, and o). *ifa-4(ok1734)* and *exc-2(rh90)*, presumed null alleles of *ifa-4* and *ifc-2*, respectively (http://www.wormbase.org; Al-Hashimi et al., 2018), displayed a similar milder phenotype (Fig. S1, m–o; *exc-2(rh90)* is designated *ifc-2(rh90)* below for clarity). Some *ifa-4-, ifb-1-, ifc-2(RNAi)*, and mutant animals arrested at the early L1/L2 larval stage with the canonical excretory canal Clr phenotype (fluid-filled body; Nelson and Riddle, 1984) suggesting nonfunctional canals. This L1-lethal phenotype became fully penetrant in ERM-1^{++} *ifb-1(RNAi)* double mutant/RNAi animals (Fig. S1, d–g). We conclude that of 11 *C. elegans* cIFs, 3 (IFA-4, IFB-1, and IFC-2) affect canal tubulogenesis, and all 3 affect canal lumenogenesis and interact with ERM-1 in this function.

IFA-4, IFB-1, and IFC-2 abut ERM-1 at the lumen, and their conditional removal uncovers a requirement for lateral growth during intracellular lumen extension

To systematically assess cIF function in ERM-1–dependent canal lumenogenesis, we determined the subcellular and developmental expression pattern of all canal cIFs and their isoforms and their spatial relation to each other and to ERM-1. Prior studies suggested that IFA-4, IFB-1, and IFC-2 are expressed in excretory canals, with IFA-4 and IFC-2 thought to overlap lumenal ERM-1 (Karabinos et al., 2003; Woo et al., 2004; Kolotuev et al., 2013; Al-Hashimi et al., 2018). We found that the two isoforms IFB-1A and IFB-1B, fused to GFP and directed by their own promoters, were similarly expressed in canals, albeit

Khan et al.
A tensile endotube propels intracellular lumens

Journal of Cell Biology
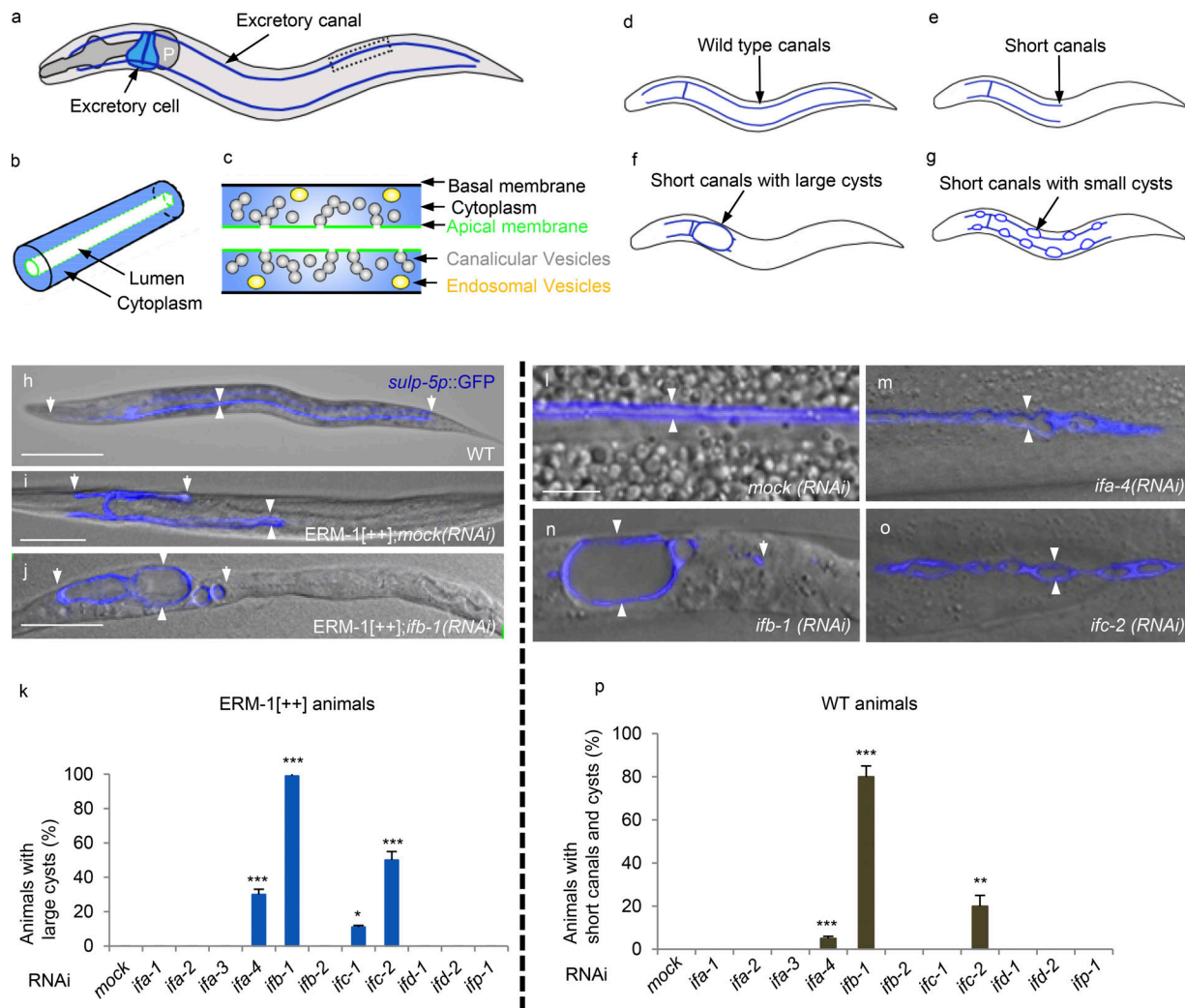https://doi.org/10.1083/jcb.201811175

2404

Figure 1. A genetic modifier screen independently identifies three cIF genes as functionally interacting with *erm-1* in *C. elegans* excretory canal morphogenesis. Compare with Fig. S1. **(a–c)** Schematics of WT canal. **(a)** Whole animal with a single canal cell and fully extended canals. **(b)** 3D view of canal arm section (boxed in a). **(c)** 2D view of subcellular components. **(d–g)** Schematics of WT and prototypic mutant canals. **(h–k)** ERM-1^{++} small cystic and short canals are enhanced by *ifa-4-*, *ifb-1-*, *ifc-1* and *ifc-2* RNAi (see Materials and methods for quantification of cyst size and canal length). Bar graph shows comprehensive analysis of the effects of cIFs on ERM-1^{++} canals. **(l–p)** IFA-4, IFB-1, and IFC-2 are required for WT canal morphogenesis. Note the large, cell-body close cyst without canal extension in *ifb-1(RNAi)* animals (n and f) versus grapes-on-a-vine cysts on shortened canals in *ifa-4(RNAi)* (m and g) and *ifc-2(RNAi)* animals (o and g). Single posterior canal arm sections are shown. Bar graph shows comprehensive analysis of the effects of cIFs on WT canal morphogenesis. Arrows indicate canal tips (posterior tip in n) and arrowheads bracket canal width. Scale bars represent 100 µM in (h–j) or 20 µM (l–o; shown in l). Unless indicated otherwise, images in Figs. 1–10 show confocal and confocal Nomarski overlay images of whole animals or single posterior canal arm sections, with the canal cytoplasm in blue (pseudocolored from P$_{sulp-5}$::GFP or P$_{sulp-5}$::mCherry) and canal lumen and subcellular components in red or green. Animals are positioned with anterior left, posterior right, dorsal top, and ventral bottom; P indicates the posterior pharynx bulb (location of canal cell body). Data in this and all other figures are presented as mean ± SD (*n* > 3). *, P < 0.05; **, P < 0.001; ***, P < 0.0001 (*t* test). See text for details of all data shown.

differentially in other tissues (Fig. 2, a–d; and Fig. S2, d–f; Woo et al., 2004). Both IFB-1A and IFB-1B were absent at lumen initiation and first appeared in laterally extending canals, where they persisted through anterior–posterior canal extension and thereafter (Fig. 2, a–d'). Double-labeling canals with cytoplasmic mCherry localized both GFP-labeled isoforms to the lumen (Fig. 2, e–e'; and not shown). IFA-4 has one isoform, whereas IFC-2 has four, two of which (IFC-2A and IFC-2B) are relevant to canal development (Fig. S2, a–c; Al-Hashimi et al., 2018). By confocal microscopy, lumenal canal membranes are only discernable as doublet from the L3/L4 stage onward (Khan et al., 2013; Zhang et al., 2017b). To optimize comparative imaging of

all canal cIFs and their isoforms during canal lumenogenesis, *ifa-4*, *ifb-1b*, *ifc-2a*, and *ifc-2b* cDNAs were cloned behind the canal-specific *sulp-5* promoter and fused to different fluorophores. All localized to expanding larval and fully expanded adult lumenal membranes (Fig. 2, f–h"; Fig. S2, g and h; and not shown) adjacent to but distinct from lumenal ERM-1 (Fig. 2, i–k"). Thus, all *C. elegans* canal cIFs and their isoforms are located at the lumen, albeit outside of ERM-1, consistent with their shared function in canal morphogenesis via either lumen development or maintenance, but not lumen initiation.

Cysts are terminal canal phenotypes caused by various injuries (Zhang et al., 2017b). To generate informative IF
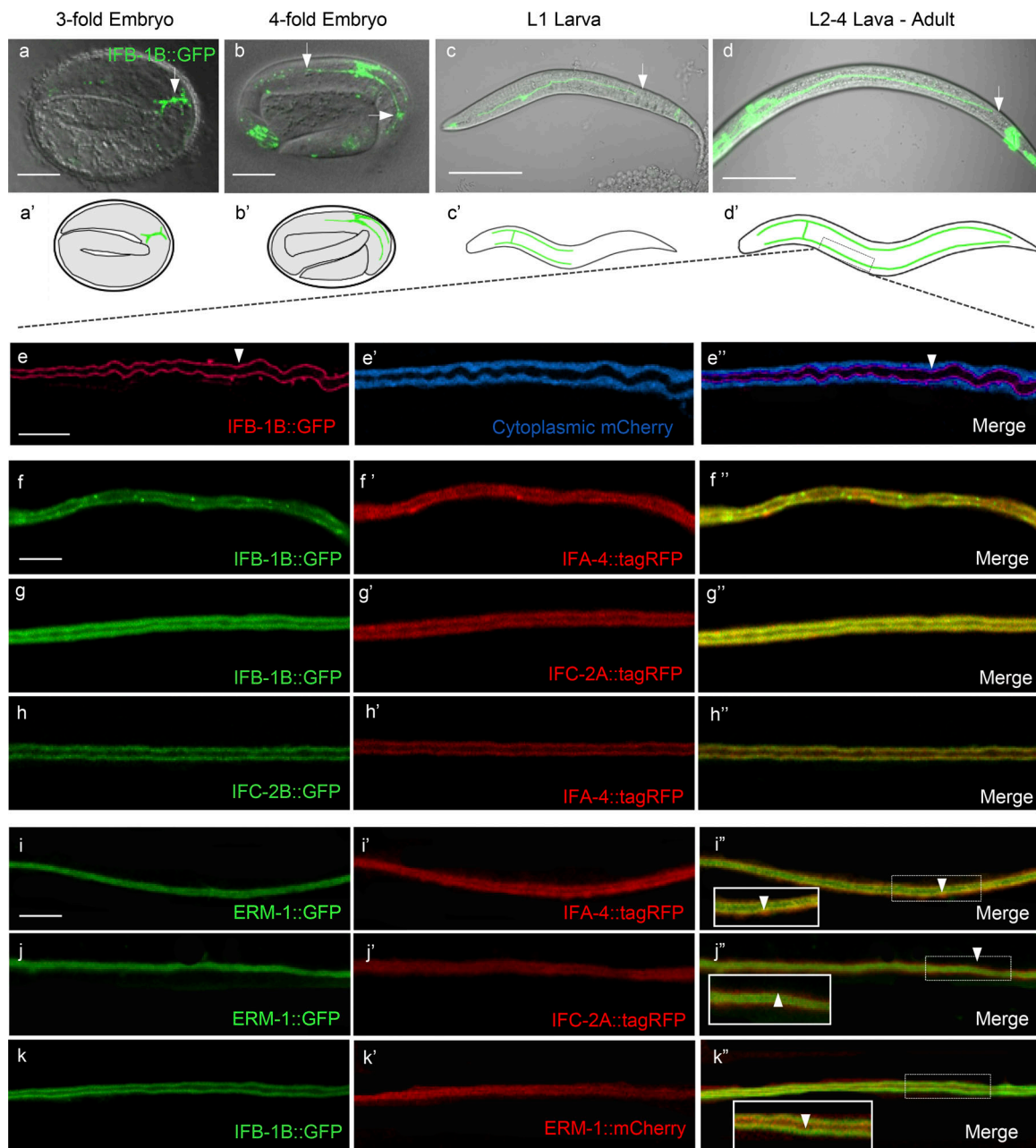
Figure 2. **IFA-4, IFB-1, and IFC-2 overlap with each other and abut ERM-1 at growing apical/lumenal membranes in canals.** Compare with Fig. S2. **(a–d')** Developmental cIF expression. IFB-1B expression starts with canal extension and persists into adulthood. Canals reach nose and tail in L2; arrows indicate canal in panel a and canal tips in b–d. Corresponding schematics are shown below images. **(e–k")** cIF expression in a single larval canal arm (boxed in d") and lumenal endotube sections (f–k"). **(e–e")** IFB-1B is localized at the lumen (arrowhead; IFB-1::GFP pseudocolored to red in these images). **(f–h")** IFA-4, IFB-1, and IFC-2A/B colocalize. **(i–k")** Lumenal IFA-4, IFB-1, and IFC-2A abuts lumenal ERM-1 at the cytoplasmic side. Note the green-red boundaries in i", j", and k" (arrowheads in magnified insets of boxed areas) versus the yellow overlap in f", g", and h". L3–L4 canals are shown (see Materials and methods). Image background is blackened in i–i", j, k', and k" for clarity (see Fig. S5, 2I–I", 2J, 2K', and 2K", for corresponding originals). Scale bars represent 10 µM (a and b), 100 µM (c and d), and 10 µM (in e for e–e", f for f–h", and i for i–k").

loss-of-function canal phenotypes and determine if IFs primarily affect canal morphogenesis or, as previously claimed, secondarily affect it by maintaining the canal's structural integrity (Carberry et al., 2012; Kolotuev et al., 2013; Al-Hashimi et al., 2018), we selectively depleted IFs at different tubulogenesis stages. Depletion in adults showed no visible defects, suggesting that IFs are dispensable for maintaining canal tube or lumen structure

(Fig. S2, i–o). In contrast, depletion in L1 larvae impaired the canals' ability to "catch up" with body length. Transient "varicosities" or "pearls" (presumed growth sites) decorate WT canal tubes at regular intervals during this active growth phase (Fig. 3, a and b; Hahn-Windgassen and Van Gilst, 2009). We identified a lateral-growth phenotype in *ifb-1(larvalRNAi)* canals, with persistent, enlarged, and fluid-filled varicosities, contrasted by thin

or seemingly absent intervening canal segments (Fig. 3, c and c′). ERM-1::GFP labeling revealed multiple, ostensibly disconnected cysts, suggesting a multiple-lumen phenotype (Fig. 3, d and d′). *ifa-4(larvalRNAi)* and *ifc-2(larvalRNAi)* produced a similar, although weaker, multicystic lateral-growth phenotype (not shown). *ifb-1-*, *ifa-4-*, and *ifc-2(larvalRNAi)* varicosity cyst aggregates resembled *ifa-4(ok1734)* and *ifc-2(rh90)* mutant grapes-on-a-vine cyst pattern (Figs. S1, m–o; also compare Fig. 3, l, o, and p). Of note, similar cyst aggregates can also trail *ifb-1(fullRNAi)* large cell-body close cysts (Fig. 1 n and Fig. S1, c, k, and l). Collectively, these findings suggest that the three IFs all directly function in canal (specifically canal lumen) morphogenesis, not in maintenance, and that it is the disruption of this same specific IF function that causes all IF loss-of-function canal phenotypes.

To examine the contiguity of IF-depleted canals and lumens, we serially sectioned *ifb-1(larvalRNAi)* canals with persistent varicosities by transmission electron microscopy (TEM). The analysis revealed thin meandering lumens between cysts inside varicosities but no lumen structure above canalicular size in thin canals between varicosities, suggesting that canals but not lumens were contiguous (Fig. 3, i–n). It is not known how canals and lumens extend. We considered that lumens might independently arise in varicosities and bidirectionally connect in an IF-dependent process. Alternatively, IF-depleted canals or lumens might rupture during canal extension (suggested in Kolotuev et al., 2013). To distinguish between these possibilities, we examined tubulogenesis in real time, tracing canal tube extension with P$_{sulp-5}$::GFP and canal lumen extension with excess ERM-1::GFP (designated ERM-1::GFP[++]), titrated to the highest signal strength compatible with lumen integrity. These studies demonstrated unidirectional canal and lumen growth in both WT and IF-depleted animals, with ERM-1::GFP[++] uncovering ultrathin lumen bridges between varicosities, contrasted by a tortuous multicystic lumen course in varicosities and at canal tips (Fig. 3, e–h). We conclude that *C. elegans* canal and canal lumen extension is unidirectional and must integrate lateral growth from interspaced varicosities. We further conclude that IFs restrict excess lateral lumen growth and cyst formation while driving the lumen forward. IFs thus have an active morphogenetic function in capillarogenesis rather than passively maintaining canal or lumen structure.

AFs and MTs functionally interact with IFs in intracellular lumenogenesis

AFs and MTs coordinate *C. elegans* canal and lumen tip growth (Shaye and Greenwald, 2015), but their function in the process of lumen formation and extension is not known. We next examined whether the IF function in canal lumenogenesis was dependent on AFs and MTs. ACT-5/cytoplasmic-actin and F-actin–binding LifeAct are enriched at the canal lumen (Khan et al., 2013; Shaye and Greenwald, 2015). We generated a TBB-2/ β-tubulin::GFP fusion protein and found it localized to both the canal cytoplasm and lumen, similar to the MT-binding EMTB (see Fig. 7, c and d; Richardson et al., 2014). To distinguish the roles of these three cytoskeletal filaments in canal versus lumen extension, we analyzed animals double-labeled with cytoplasmic and lumenal canal markers. ERM-1 binds to and recruits ACT-5

to the canal lumen (Khan et al., 2013). Interference with AFs (via *act-5* RNAi) copied the *erm-1(RNAi)* phenotype and fully aborted canal extension and lumen formation (Fig. 4, a and b). In contrast, interference with IFs (via *ifb-1* RNAi) and MTs (via *tbb-2* RNAi) allowed for the initiation of lumen and canal morphogenesis but generated short canals with lumenal cysts (Fig. 4, f and g). *act-5* (or *erm-1*) RNAi, when initiated in larvae, halted canal and lumen extension, leaving stunted remnants of both (Fig. 4, c–e; and Fig. S3 a). In contrast, *tbb-2* larval RNAi copied the *ifa-4-*, *ifb-1-*, and *ifc-2(larvalRNAi)* lateral-growth phenotype with multicystic lumens in varicosities and thin intervaricosity lumen segments (Fig. 4, h–j; and Fig. S3 b). These findings suggest that AFs and IFs function in different, and MTs and IFs in similar, aspects of capillary-like lumenogenesis. They also identify a new role of tubulin in *C. elegans* canal lumenogenesis.

We next examined genetic interactions among AFs, IFs, and MTs and evaluated actin and tubulin's ability to modify the moderately severe multicystic *ifa-4(ok1734)* lumen phenotype (Fig. 4, k–t). *ifa-4(ok1734)* deletes exons 6 and 7 and introduces a premature stop (Fig. S2 a). Unexpectedly, mild *act-5* RNAi, allowing partial lumen extension, suppressed *ifa-4(ok1734)* cystic lumens (Fig. 4, k–m), consistent with an antagonistic AF–IF relationship in lumenogenesis. Mild ERM-1 depletion similarly suppressed *ifa-4(ok1734)* cystic lumens (Fig. 4, n–p), suggesting that the loss of lumenal, but not cytoplasmic, actin mediated suppression. In contrast, mild TBB-2 depletion enhanced *ifa-4(ok1734)*, inducing large, *ifb-1(RNAi)*–similar cysts without any lumen extension, consistent with a synergistic MT/IF function in lumenogenesis (Fig. 4, q–s).

tbb-2 RNAi's ability to enhance the *ifa-4(ok1734)* null allele suggested that MTs act in parallel to IFA-4. To further examine the MT–IF interaction, TBB-2 was also depleted in the *ifc-2(rh90)* null allele (Fig. S2 c). *tbb-2* RNAi failed to enhance this allele, consistent with a direct interaction with IFC-2. Surprisingly, however, it suppressed the *ifc-2* phenotype (Fig. 4 t). Together, these results suggest that tubulin depletion indirectly enhances IFA-4 loss via tubulin's direct effect on IFC-2, whose loss it cannot further enhance. Additionally, tubulin must have an independent, IF-antagonistic function in lumenogenesis (resulting in *ifc-2(rh90)* suppression) revealed by the loss of a single IF (e.g., IFC-2) but masked by the severe phenotype induced by loss of two (e.g., IFA-4 and IFC-2; Fig. S3, c and d, schematic).

We conclude that all three cytoskeletal elements cooperate in excretory canal lumenogenesis. AFs form (initiate and extend) the lumen, while IFs and MTs shape it into forward extension. The antagonistic yet shared lumenogenesis function of AFs versus IFs/MTs suggests that the latter modify a process initiated by the former.

AFs and MTs recruit endosomal and canalicular vesicles to the lumen, where IFs restrain their respective fusion and docking

Both actin and tubulin have been implicated in intracellular lumenogenesis via vesicular trafficking, and IFs can provide vesicle tracks (Rao et al., 2011; Khan et al., 2013). We therefore next examined if the three cytoskeletal filaments might cooperate in lumenogenesis via distinct functions in vesicular trafficking. *C. elegans* canal lumen extension requires vesicle
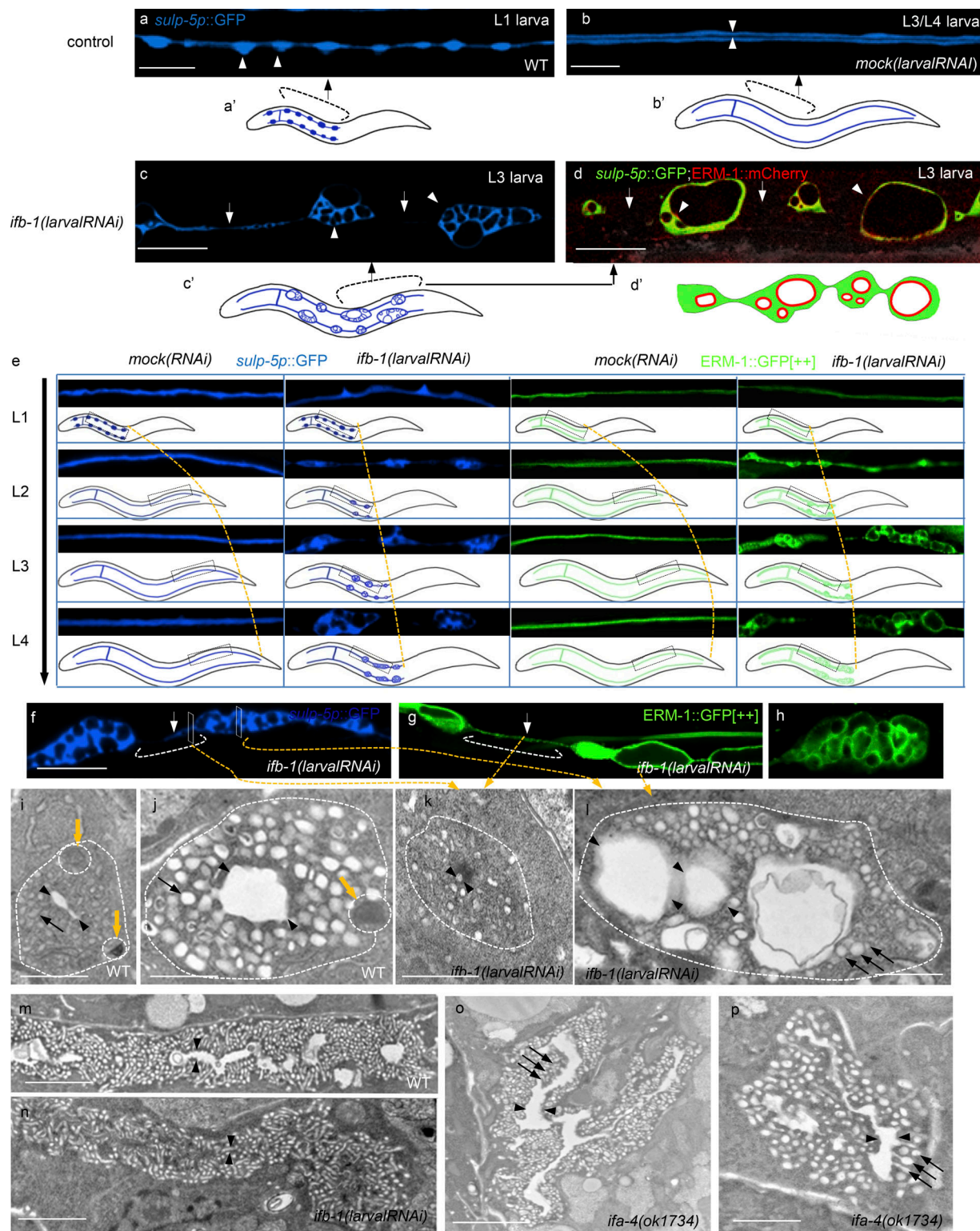
Khan et al.
A tensile endotube propels intracellular lumens

Journal of Cell Biology
https://doi.org/10.1083/jcb.201811175

2407

Figure 3. **The three canal IFs extend the intracellular lumen by restricting lateral growth and cystogenesis. (a–d)** Larval IFB-1 depletion causes a tortuous multicystic varicosity phenotype. **(a–b')** WT larval canal arms and corresponding schematics. Interspaced lateral growth sites (varicosities; arrowheads in a) in extending L1 larval canal are integrated in L3/L4 canals (lumen now discernable; arrowheads in b; arrows in a' and b' indicate segments of the corresponding schematic). **(c–d')** *ifb-1(larval RNAi)* L3 larval canal arms and corresponding schematics. Persistent, enlarged varicosities with cystic structures (arrowheads) and thin or missing intervaricosity canal sections (arrows); lumenal ERM-1 (red) identifies cystic structures as lumens that appear to be disjunct (d and d', late phenotype with coalescing cysts/lumens; cytoplasm shown in green for clarity). **(e–h)** Real-time canal and lumen extension. Canals and lumens extend unidirectionally and remain intact after *ifb-1* larval RNAi. Canal tubes labeled with P~sulp-5~-GFP and canal lumens labeled with overexpressed ERM-1 (ERM-1:: GFP[++]) were traced during L1–L4 larval canal extension. Boxed areas in schematics (bottom) shown on top (see Fig. S5, panel 3E, for uncropped images). Note

truncated forward growth of *ifb-1(larvalRNAi)* canals and lumens (dotted yellow lines) but excess lateral growth (meandering multicystic lumens in enlarged varicosities and at canal tips; f–h). Images show ultrathin but intact *ifb-1(larvalRNAi)* intervaricosity canal and lumen sections (arrows in f and g) and a meandering ERM-1::GFP[++]–labeled lumen tip (h). Dotted arrows lead to corresponding TEM micrographs below. **(i–p)** TEM micrographs of serially sectioned WT and IF-depleted canals. Cross sections (i–l) and sagittal sections (m and n) of WT versus *ifb-1(larval RNAi)* varicosities (j and l) and intervaricosity (i, k, m, and n) canal arm segments are shown. Note that the lumen (bracketed by arrowheads) is not separable from canaliculi in k and n (a lumen is only presumed in k and n; compare to i and m). Connections between cysts in l and lumens in m are outside the section. **(o and p)** Tangential cross sections reveal connected but meandering lumens in IFA-4 mutant canals. Canal boundaries are outlined by dotted lines in i–l; all endosomal vesicles (circled, yellow arrows) and some canalicular vesicles (black arrows) are indicated in i, j, o, and p. Not all lumen cysts/branches are bracketed by arrowheads in l, o, and p. Note the missing endosomes in k, l, o, and p and clustering of canaliculi in l, o, and p (arrows). Image background is blackened in some panels in e for clarity (see Fig. S5, panel 3E, for corresponding originals). Scale bars represent 30 µM (a–d), 15 µM (in f for f–h), and 1 µM (i–p).

coalescence (Khan et al., 2013; Armenti et al., 2014). Several endosomal vesicle populations function in canal lumenogenesis, among them RAB-5, RAB-7, and RAB-11⁺ endosomes (Mattingly and Buechner, 2011), but it is not known if they expand the lumenal membrane. We thus first examined their function in WT canal lumenogenesis and found that *rab-5*, *rab-7*, and *rab-11* RNAi fully aborts ERM-1::GFP-tagged lumenal membrane expansion and thereby lumenogenesis (Fig. 5, a–d). We conclude that endosomal trafficking is strictly required for canal lumen extension, supporting an intracellular lumenogenesis model that is based on endosomal membrane delivery (Khan et al., 2013).

We next depleted each of the three IFs either fully or conditionally during larval extension and assessed its effect on mCherry::RAB-5, mCherry::RAB-7, and mCherry::RAB-11⁺ canal endosomes. Unexpectedly, their depletion severely reduced the numbers of all three endosomes (IFB-1 depletion most severely), suggesting they were consumed in cyst membranes (Fig. 5, e–k; Fig. S3, e–n; and not shown). Consistent with this conclusion, *ifa-4(ok1734)* cysts were suppressed and canals reextended when treated with mild *rab-5*, *rab-7*, and *rab-11* RNAi, titrated to allow for lumen extension (Fig. 5, x–z3). In striking contrast, mild *erm-1*, *act-5*, and *tbb-2* RNAi increased the size and number of these endosomes, suggesting they were no longer incorporated into the lumenal membrane (Fig. 5, e–g and l–w). *erm-1* and *act-5* RNAi caused endosomes to randomly cluster, whereas *tbb-2* RNAi chiefly led to their aggregation along basal membranes, suggesting that MTs specifically recruit endosomes from basal to apical/lumenal membranes. Endosomal vesicles were not affected by interference with other structural components of the lumenal endotube, such as the spectrin cytoskeleton (Fujita et al., 2003; Fig. S3, k–n). Thus, IFs restrict, and AFs/MTs promote, vesicle access to the lumen, consistent with an antagonistic function of IFs versus AFs/MTs and suggesting a mechanism for the suppression of IF-dependent cysts by *erm-1* and *act-5* RNAi. Furthermore, tubulin is identified as another cytoskeletal component promoting canal lumenogenesis via vesicle recruitment, the likely basis for the suppression of *ifc-2(rh90)* cysts by *tbb-2* RNAi (Fig. 4 t).

Next, we examined canal-specific canalicular vesicles that, unlike single-standing endosomal vesicles, form pancytoplasmic tubulovesicular networks in dynamic exchange with the canal's lumenal membrane (Fig. 1 c). They are also recruited to, but not integrated into, the lumenal membrane by ERM-1, where they support lumen extension via aquaporin-regulated translumenal flux (Khan et al., 2013). Unlike endosomal vesicles, upon IF depletion, AQP-8/aquaporin–labeled canalicular vesicles were not

consumed but accumulated at expanding cyst membranes, most conspicuously in varicosities, suggesting they might drive cystogenesis via translumenal flux (Fig. 6, a and b). Indeed, by depleting AQP-8, or inhibiting its water channel activity by mercury, cyst size and number were suppressed in *ifb-1(RNAi)* and *ifa-4(ok1734)* canals (Fig. 6, c–j), whereas AQP-8 overexpression enhanced *ifb-1(RNAi)* cysts and larval lethality (Fig. 6, k–n). In contrast, *erm-1*, *act-5*, and *tbb-2* RNAi retained AQP-8::GFP-labeled canalicular vesicles in the cytoplasm (Fig. S4, a and b; Khan et al., 2013).

Combined, our findings suggest that actin and tubulin recruit endosomal and canalicular vesicles to the lumen, where their fusion (endosomes) and docking (canaliculi) are spatially regulated by IFs. Lumenal membrane addition and translumenal flux, prerequisites for lumenogenesis, are thus laterally restrained, causing the lumen to extend forward. Tubulin serves two functions in intracellular lumenogenesis, one synergistic with actin (vesicle recruitment) and the other synergistic with IFs (restraining lateral expansion).

Recruitment of IFB-1 to an intracellular perilumenal cytoskeleton depends directly on TBB-2 and indirectly on ERM-1

Shape-forming cIF networks typically connect to AFs and MTs (Huber et al., 2015). To dissect the unusual perilumenal assembly of three IFs, we first defined the spatial relationship between IFs and lumenal actin and tubulin. Our data place IFB-1::GFP adjacent to but outside of lumenal ACT-5::GFP via the latter's overlap with ERM-1 (Fig. 7, a–b'") and adjacent to but inside of lumenal TBB-2::GFP or EMTB::GFP (Fig. 7, c–d'"). The submembranous canal lumen cytoskeleton thus has three concentric layers: AFs surrounded by IFs surrounded by MTs (Fig. 7 e).

We next examined whether IF, AF, and MT's intracellular perilumenal assembly was interdependent. Canal lumenogenesis can be arrested at various stages without aborting lumen formation by titrating *erm-1* RNAi, allowing the visual dissection of its molecular assembly (Khan et al., 2013). Disrupting lumenal membrane expansion by moderately severe *erm-1* RNAi displaced IFB-1 to the cytoplasm, demonstrating that lumenal assembly of IFB-1 requires ERM-1 (Fig. 7, f and f'). Conversely, ERM-1 and actin remained lumen-close in the absence of IFs (Fig. S1, h–k and o). Disrupting lumenal vesicle recruitment by mild-to-moderate *erm-1* RNAi permitted partial IF recruitment to coalescing vesicles, trapping mCherry::RAB-7⁺ vesicles outside a loose IFB-1 web, consistent with the role of IFs in restricting vesicle access to the nascent lumen (Fig. 7 g).
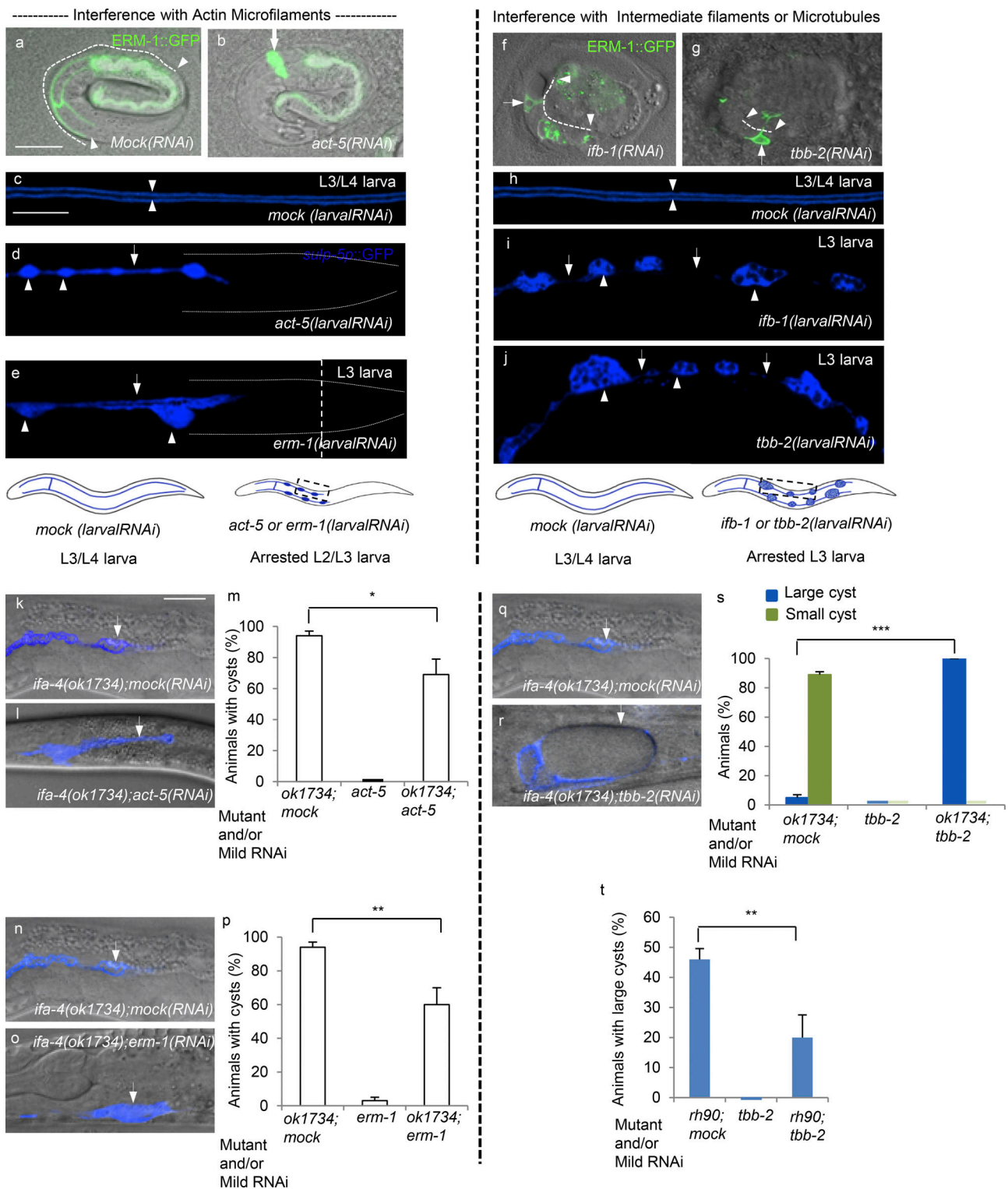
Figure 4. **AFs and MTs interact with IFs in excretory canal lumenogenesis. (a–e)** AFs. **(b)** Parental *act-5* RNAi fully aborts lumenogenesis in embryos. The ERM-1::GFP-labeled intestinal lumen is greyed out for clarity. **(c–e)** Larval *act-5* and *erm-1* RNAi halt canal and lumen extension in L2/L3 larvae. Note the intervaricosity sections with uniform canal diameters (d and e; compare to the thin intervaricosity sections in i and j; arrows) and uniform lumen diameters (absent in d; pearls-on-a-string pattern in e) in fully truncated canals (compare to i and j). See Fig. S3 a for quantification. **(f–j)** IFs and MTs. **(f and g)** Parental *ifb-1* and *tbb-2* RNAi produce cystic short lumens in embryos. **(h–j)** Both larval *ifb-1* and *tbb-2* RNAi generate the multicystic varicosity phenotype in L3 larvae (compare with Fig. 2). Note seemingly absent intervaricosity canal sections and lumens (arrows) between enlarged cystic varicosities (arrowheads). See Fig. S3 b for quantification. Dotted lines show canal lumen arm length (a, f, and g) and animal outline (d and e); arrowheads show lumen tips (a, b, f, and g), lumen width (c and h), and persistent varicosities (d, e, i, and j); and arrows show canal cell body without lumen extension (b), lumen cyst (f and g), and intervaricosity canal section (d, e, i, and j). Images in c–e and h–j show boxed areas in corresponding whole-animal schematics below. **(k–p)** Genetic IF/AF interactions in canal

lumenogenesis. Mild *act-5* RNAi (k–m) and *erm-1* RNAi (n–p) suppress *ifa-4(ok1734)* cysts. **(q–t)** Genetic IF/MT interactions in canal lumenogenesis. Mild *tbb-2* RNAi enhances *ifa-4(ok1734)* cysts (q–s) and suppresses *ifc-2(rh90)* cysts (t). See Fig. S3, c and d, for model. The same images are shown for *ifa-4(ok1734)* controls in k, n, and q. Representative single canal arm sections (arrows) are shown in k, l, n, o, q, and r. Scale bars represent 20 µM (in a for a, b, f, and g; c for c–e and h–j; and k for k, l, n, o, q, and r).

Disrupting lumenal vesicle alignment by mild *erm-1* RNAi revealed an intriguing IFB-1 assembly into a centered braid, consistent with the proposed role of IFs as spatial organizers at the vesicle–lumen interface (Fig. 7 h). ERM-1 overexpression failed to increase lumenal IFB-1 levels (Fig. 7, i–k). Combined, these results suggest that ERM-1 indirectly recruits IFs to the lumen, where IFs in turn modify (restrain) ERM-1's function in vesicle coalescence. This conclusion is consistent with the observed antagonistic ERM-1–IF interaction (IF depletion enhanced ERM-1 [++] cysts; ERM-1 depletion suppressed IF[−] cysts).

In contrast, mild *tbb-2* RNAi was sufficient to displace IFB-1 from the lumen (Fig. 7, l and l′), and an increase in transgenic *tbb-2* copies expanded the lumenal IF coat (Fig. 7, m–o; and Materials and methods). Conversely, *ifb-1* RNAi did not displace TBB-2 from the lumen but did expose its spiral configuration around expanded cyst membranes (see Fig. 9, m and m′). We conclude that the perilumenal assembly of IFs directly requires TBB-2, consistent with the synergistic IF–MT interaction and their similar loss-of-function phenotypes and suggesting that the dominant function of MTs in intracellular lumenogenesis is mediated by IFs. Consistent with the second IF-antagonistic lumenogenesis function of MTs in vesicle recruitment, *tbb-2(RNAi)* clustered mCherry-RAB:11 vesicles at basal canal membranes despite IF loss at the lumen that should have resulted in their consumption (Fig. 7 l′).

The trilayered cytoskeletal endotube contains a tensile triple IF lattice embedded between lumenal AFs and helical MTs
To analyze the structure–function relationship of the perilumenal triple IF assembly, we first examined the genetic interactions among IFs during canal lumenogenesis. In combination, the *ifa-4(ok1734)* and *ifc-2(rh90)* null mutants enhanced their respective small-cystic, short canal lumens to *ifb-1(RNAi)*-specific large cysts, with an absence of canal/lumen extension and increased lethality (Fig. 8, a–i′; and Fig. S4, c–h), consistent with IFA-4 and IFC-2 acting in parallel. Double-null mutants could not, however, be further enhanced by larval *ifb-1* RNAi (Fig. 8 g), revealing that the combined IFA-4/IFC-2 function directly requires IFB-1. Moreover, *ifa-4(ok1734)* and *ifc-2(rh90)* were each similarly enhanced by larval *ifb-1* RNAi to the *ifa-4(ok1734) ifc-2(rh90)* double or full *ifb-1(RNAi)* phenotype, suggesting each was enhanced by the parallel effect of IFB-1 loss on the other. These findings are consistent with IFB-1 associating independently with each IFA-4 and IFC-2, while all three IFs combine in a functional higher-order assembly.

cIFs build complex networks with tensile properties (superstructures) in successive steps that include dimerization, filament formation, and polymerization into bundles and higher-order assemblies (Chang and Goldman, 2004; Block et al., 2015). In vitro, *C. elegans* IFB-1A physically interacts with IFA-1–IFA-4 and IFC-2, and failure of heterodimerization causes aggregation

(Karabinos et al., 2003). We next asked whether lumenogenesis function of IFs required filament formation in vivo. Indeed, treatment with AlCl3, shown to inhibit in vivo filament formation (Kushkuley et al., 2010), dose-dependently disrupted *C. elegans* canal extension and enhanced *ifa-4(ok1734)* cysts (Fig. S4, i–k). We considered that the occasionally observed aggregation of GFP-tagged IF fusion proteins, rather than reflecting GFP-derived artifacts, might result from defective filament formation due to imbalances in IF stoichiometries. We therefore assessed whether the loss of single IFs affected aggregation of the others. IFB-1 depletion in fact increased the number and size of IFA-4 and IFC-2 aggregates (whether fused to GFP or tagRFP), whereas IFA-4 or IFC-2 depletion had no effect (Fig. 8, j–w; IFB-1::GFP background aggregates precluded the analysis of inverse scenarios). This set of experiments also demonstrated that neither IF was required to recruit the other to the lumen. We thus expect IFB-1 to associate with IFA-4 and IFC-2 independently and before filament formation, suggesting that IFB-1/IFA-4 and IFB-1/IFC-2 heterodimerize in vivo during lumenogenesis.

We next compared the spatial relationships among the three IFs at canal lumens by high-resolution confocal microscopy (Materials and methods). IFs displayed a web pattern with gaps of roughly pentagonal shape, consistent with a higher-order IF assembly into a perilumenal lattice (Fig. 9, a–c and g–j). No single IF loss altered the structure of the others or fractured the lattice, but loss of each stretched the gaps around cysts, confirming the lattice structure and revealing its tensile properties (Fig. 9 c and not shown). IFA-4::GFP, IFB-1::GFP, and IFC-2::GFP lattices were superimposable in triple IFA-4::GFP–, IFB-1::GFP–, and IFC-2::GFP–labeled canals, consistent with a contribution of each IF to all lattice strands (Fig. 9 j). IFB-1::GFP strands directly abutted IFA-4::tagRFP and IFC-2::tagRFP (Fig. 9, g–h″), whereas the latter strands were slightly staggered (Fig. 9, i–i″), suggesting that presumed IFB-1/IFA-4 and IFB-1/IFC-2 filaments also self-associate while forming distinct parallel bundles or higher-order structures inside the triple IF lattice (Fig. 10, inset). Collectively, our results suggest that IFA-4, IFB-1, and IFC-2 are components of a triple perilumenal lattice, each indispensable, and IFB-1 critical, for structure and function.

Comparative high-resolution imaging of perilumenal AFs, IFs, and MTs revealed their distinct structural assemblies and tolerance for cystic membrane expansion. In contrast to the well-maintained fenestrated IF lattice, the smooth AF membrane undercoat was transformed into stress fiber–like strands around IF-dependent cysts, indicating additional AF functions in lumen maintenance (Fig. 9, d–f). Intriguingly, MTs encircled the lumen in helical strands, a configuration fully maintained around cysts, suggesting that resilient MTs contribute to the tensile strength of this junction-less endotube (Fig. 9, l–m′). Short MT strands were also discerned between apical/lumenal and basal sides of canals, well placed to function as vesicle tracks (Fig. 9 k, arrows).
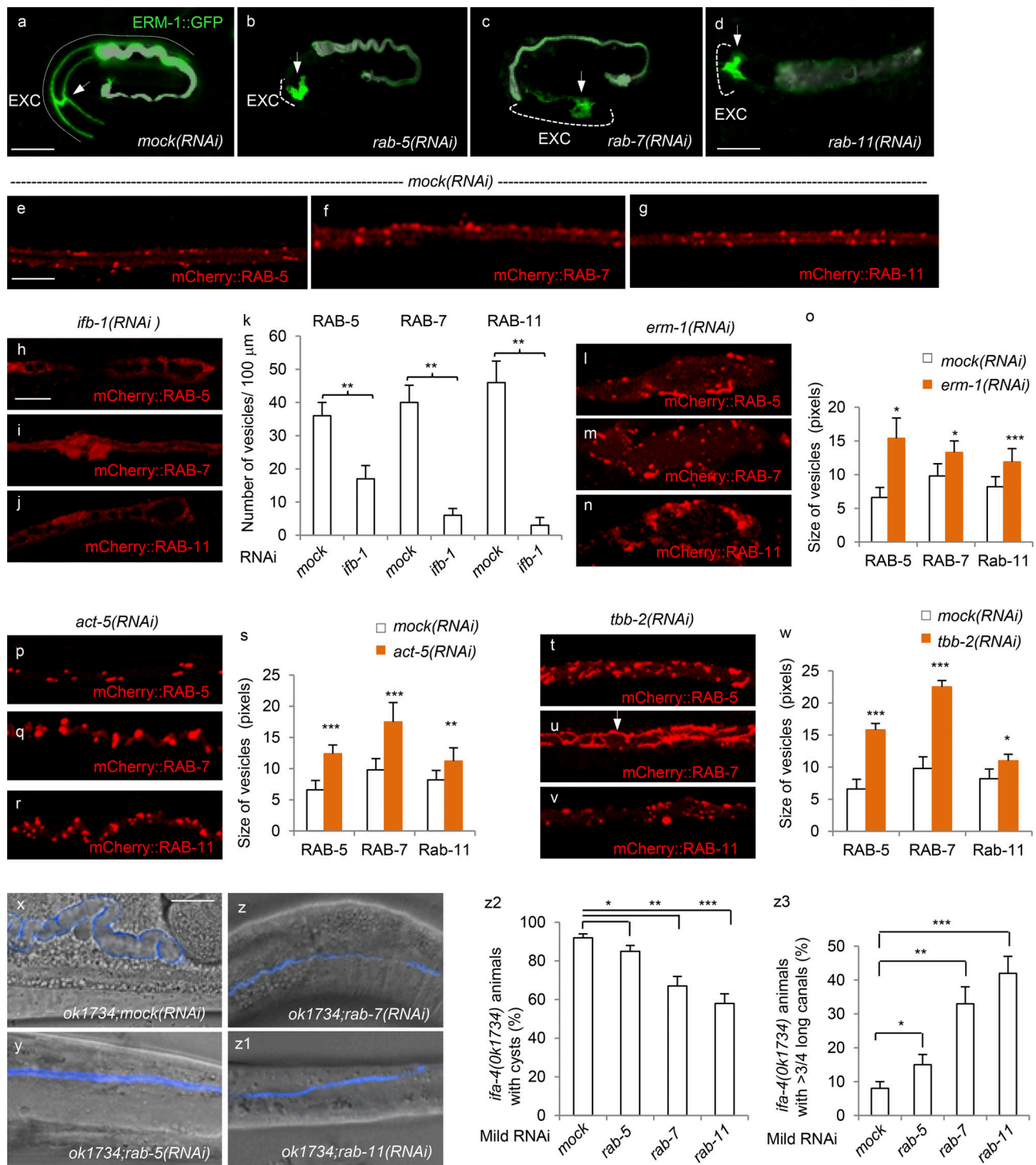
Figure 5. **Endosomal membrane delivery is strictly required for lumenal membrane expansion and is regulated by AFs, MTs, and IFs. (a–d)** RAB-5, RAB-7, and RAB-11 are required for lumenal membrane expansion. ERM-1::GFP-labeled lumenal membranes are shown in fourfold embryos (a–c) and L1 larva (d; compare with Fig. 2, b and c, for staging). Arrows show the canal cell body, and dotted lines show the extent of canal lumen extension. The intestinal lumen is greyed out for clarity. **(e–w)** RAB-5, RAB-7, and RAB-11+ endosomal vesicles (red puncta, WT; e–g) are consumed in IFB-1–depleted cystic canals (h–j) but accumulate in ERM-1– (l–n), ACT-5– (p–r), or TBB-2 (t–v)–depleted canals. Note *tbb-2(RNAi)*–specific vesicle aggregation at the basal membrane (u, arrow). Bar graphs to the right of images (k, o, s, and w) quantify vesicle number or size. See Fig. S3, e–r, for additional data and method of vesicle size quantification. **(x–z3)** Mild *rab-5*, *rab-7*, and *rab-11* RNAi suppress *ifa-4(ok1734)* cystic and short canals. Images (y–z1) show examples of fully rescued canals (most are only partially rescued). Bar graphs show quantification of cyst suppression (z2) and canal reextension (z3). Scale bars represent 15 μM (in a for a–c, e for e–g, and h for h–v), 40 μM (d), or 20 μM (in x for x–z1).
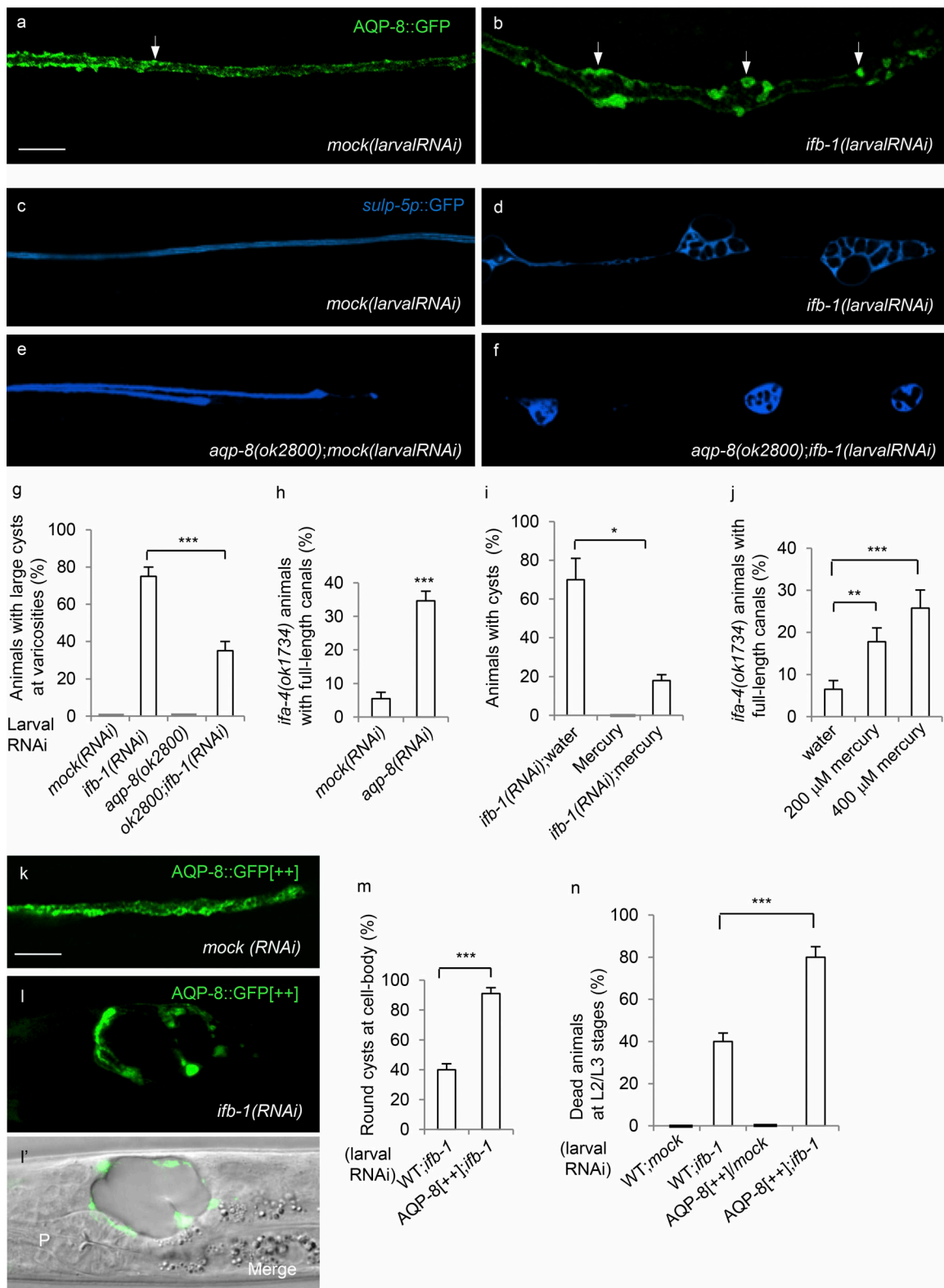
Figure 6. **Diameter equilibration of the extending canal lumen requires IF-dependent spacing of aquaporin-rich canalicular vesicles at the lumenal membrane. (a and b)** *ifb-1* larval RNAi clusters AQP-8::GFP-bearing canalicular vesicles around varicosity cysts. Compare multiple, small, homogenously distributed canalicular puncta (arrow in a; see Fig. 5, e–g, for contrasting sparse, large, irregularly distributed endosomal vesicles) to canalicular aggregates in multicystic varicosities (arrows in b). **(c–j)** Loss of AQP-8/aquaporin and disruption of its water-channel activity by mercury suppresses *ifb-1(larvalRNAi)* and *ifa-4(ok1734)* cysts and reextends canals. Note premature canal truncation in the *aqp-8(ok2800)* null allele (e) and large (d) versus small (f) cystic varicosities in *ifb-1(larvalRNAi)* versus *aqp-8(ok2800) ifb-1(larvalRNAi)* canal arm sections. **(g–j)** Quantification of suppression. **(k–n)** AQP-8 overexpression enhances *ifb-1(RNAi)* cysts and lethality. **(k–l')** Representative images of AQP-8–overexpressing transgenic line (AQP::GFP[++]) and AQP-8::GFP[++] *ifb-1(RNAi)* cysts are shown. **(m and n)** Quantification of enhancement. Scale bars represent 10 μM (in a for a–f) and 15 μM (in k for k–l').

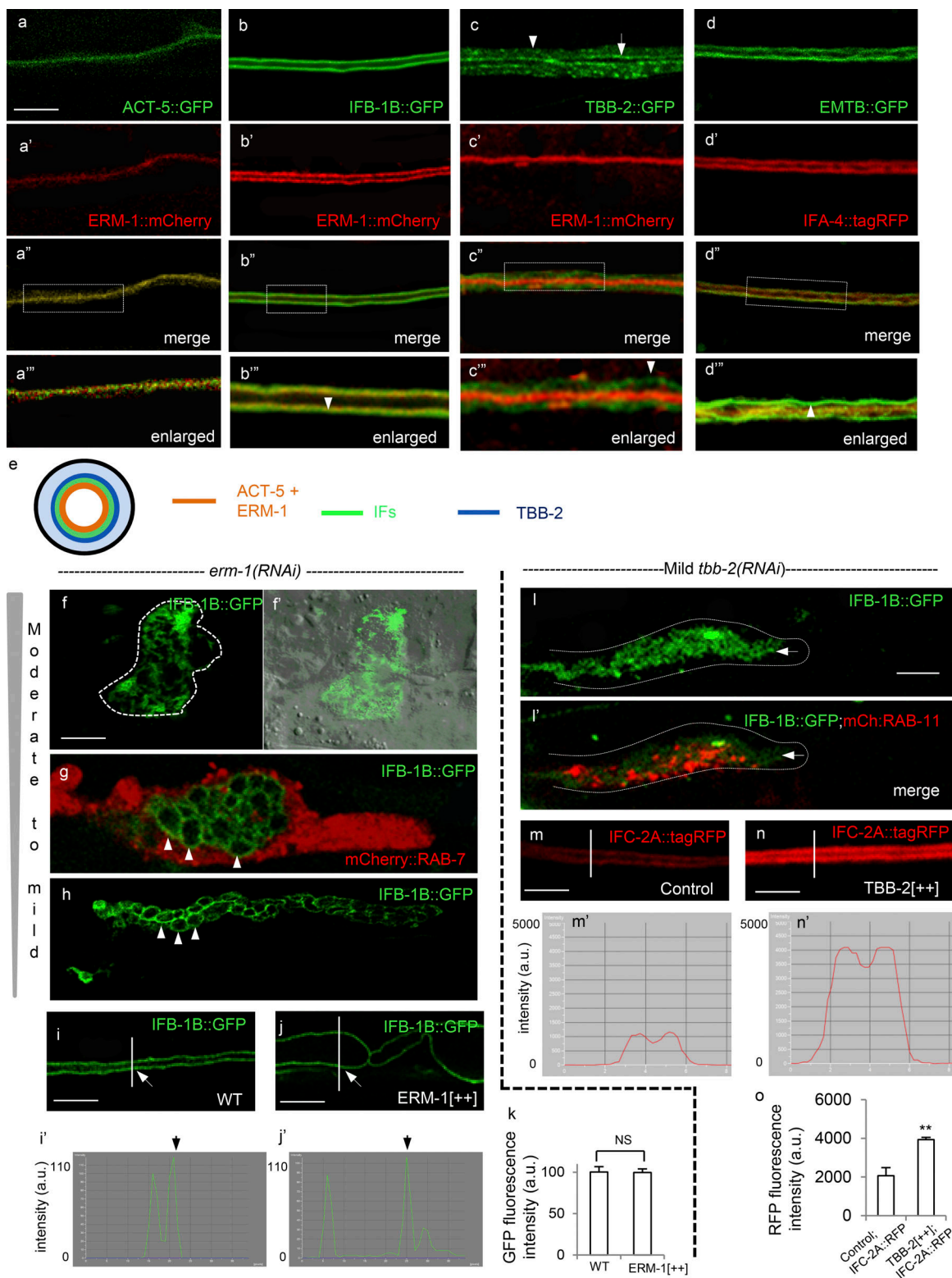Figure 7. **ERM-1 and TBB-2 recruit IFB-1 to the center of extending canals, where it forms a braid-like structure during lumenal vesicle alignment.** **(a–e)** The submembranous cytoskeleton of the intracellular canal lumen. ERM-1 overlays lumenal ACT-5 (a–a‴), surrounded by lumenal IFB-1 (b–b‴), surrounded by lumenal and cytoplasmic TBB-2 (c–c‴), and surrounded by EMBT (d–d‴; see text). Arrow points to lumenal TBB-2 (c; c and d show confocal sections focus on the lumenal MT component). Boxed areas in merged images (a″–d″) are enlarged beyond resolution to contrast overlay (a‴), adjacency (b‴, arrowhead [boundary]), distance (c‴), and proximity (d‴) of the two markers shown in each. Note spiral configuration of cytoplasmic and lumenal MT strands (arrowheads in c‴ and d‴, respectively). **(e)** Summarizing schematic. **(f–k)** ERM-1 indirectly recruits IFB-1 to the lumen. **(f–h)** Successive IF assembly during lumenogenesis (disrupted at different stages by mild-to-moderate *erm-1* RNAi): cytoplasmic IFB-1 dispersion in lumen-less canal cell (outlined by dotted line, f–f′), partial IFB-1 recruitment to coalescing vacuoles (arrowheads, g), and braid-like IFB-1 assembly around central rod during vacuole alignment (arrowheads, h).

(i–k) ERM-1 overexpression does not increase lumenal IF. Line of fluorescence intensity measurement is indicated (Materials and methods); corresponding graphs and quantification are shown below. **(l–o)** IFB-1 is directly recruited to the lumen by TBB-2. **(l and l′)** Note cytoplasmic IFB-1 dispersion and aggregation of RAB-11⁺ endosomes at basal canal membrane. Dotted line outlines canal (tip shown here); arrows show the plane of a lumen, obscured by focus on the basal membrane. **(m–o)** TBB-2 overexpression increases lumenal IFC-2 breadth and intensity (Materials and methods). Line of fluorescence intensity measurement is indicated, corresponding graphs and quantification shown below. Note that the lumen appears as a single line in L1- to L2-stage posterior canals and in L1- to L3-stage anterior canals and as a double line in older animals. An L3 anterior canal arm is shown in panel a (chosen to optimize ACT-5 canal expression; posterior canals obscured by intestinal ACT-5), posterior canal arms are shown in panels b–d (at the L3/L4 stage in panels b and d and the L2/L3 stage in panel c [chosen to optimize TBB-2 canal expression]). The image background is blackened in a–a″, b-b″, c′, c″, d–d″, g, i, and l for clarity (see Fig. S6, panels 7A–A″, 7B–B″, 7C′, 7C″, 7D–D″, 7G, 7I, and 7L, for corresponding originals). Scale bars represent 10 μM (shown in a for a–d″, f for f–h, and l for l–l′) or 5 μM (i, j, m, and n).

We conclude that IFs, MTs, and AFs assemble into distinct perilumenal structures that are compatible with their different contributions to a combined function in intracellular lumenogenesis (Fig. 10, model).

Discussion

Here, we use the unique single-cell *C. elegans* excretory canal to show how a trilayered cytoskeletal endotube tunnels a straight lumen of uniform diameter through the center of a unicellular capillary-like tube (Fig. 10, model). We propose that a tensile perilumenal triple IF lattice, embedded between AFs and MTs, laterally restrains the actin- and tubulin-dependent vesicular delivery of membrane components and fluid to the lumen. It thereby extends the lumenal endotube forward and equilibrates its diameter between interspaced sites of lateral growth (canal varicosities). These findings support a model where directed vesicle fusion and hydrostatic pressure drive intracellular lumenogenesis. They also reveal that such lumens use lateral growth to bridge unidirectional extension across long distances.

Perilumenal canal cIFs are required to extend the intracellular lumen, but not to maintain canal or lumen integrity

IF mutations cause >80 human diseases, yet the normal cellular functions of IFs remain poorly understood (Omary et al., 2004; Herrmann et al., 2007; Omary, 2009). IFs are nonpolarized filaments with resilient properties, specific to metazoans and absent in yeast and flies. Redundancies among large vertebrate IF families and a paucity of invertebrate models complicate their functional analysis. The roles of cIFs in morphogenesis are generally considered secondary to their mechanical function in maintaining tissue integrity, although dynamic cIF functions are increasingly recognized (Sanghvi-Shah and Weber, 2017; Etienne-Manneville, 2018). The prototypic higher-order cIF assembly is the pancytoplasmic filamentous network of epidermal keratins that maintains cell shape (Fuchs, 1995). The function of the occasionally polarized cortical cIFs in tubular epithelia is less clear (Oriolo et al., 2007; Iwatsuki and Suda, 2010). This study identifies a primary morphogenetic cIF function in *C. elegans* single-cell canal lumenogenesis, distinct from the proposed roles of cIFs in tissue maintenance (Chang and Goldman, 2004; Herrmann et al., 2007; Kolotuev et al., 2013; Al-Hashimi et al., 2018). The function requires the unusual polarized assembly of three cIFs—IFA-4, IFB-1, and IFC-2—here characterized as a triple perilumenal IF lattice.

The morphogenetic roles of *C. elegans* cIFs in flat and tubular epithelia are also considered secondary to structural maintenance, except for a mechanotransductory role in epidermal morphogenesis (Karabinos et al., 2001, 2003; Woo et al., 2004; Zhang et al., 2011). IFB-2 and IFC-2, polarized to the lumen of the multicellular intestinal tube, are thought to maintain the integrity of its junction-secured intercellular lumen, built between cells (Hüsken et al., 2008; Carberry et al., 2012; Coch and Leube, 2016). Likewise, cIFs were proposed to maintain the structure of the unicellular excretory canal tube and IFB-1 loss to cause cystic degeneration and rupture of its intracellular lumen (Kolotuev et al., 2013; Al-Hashimi et al., 2018). In contrast, we here show that cIFs are dispensable for canal maintenance but function directly in canal lumenogenesis. The loss of three distinct IFs does not disrupt lumen integrity but instead causes excess concentric and lateral growth at the expense of forward lumen extension. Concentric growth at lumen tips accompanies net lumen truncation, and lateral lumenogenesis at interspaced varicosities accompanies ultrathin yet intact interspaced lumen segments. The dynamic lumenogenesis function of cIFs nonetheless depends on the structural perilumenal IF assembly, revealing a new cIF structure–function relationship. The recent identification of *ifc-2* mutations in *exc-2*, one of the first described *C. elegans* cystic canal mutants, emphasizes the key role of cIFs in the *C. elegans* excretory canal (Buechner et al., 1999; Al-Hashimi et al., 2018).

The tensile perilumenal IF lattice spaces endosomal and canalicular vesicles and transforms isotropic lumen expansion into directional extension

We previously proposed that *C. elegans* canal lumenogenesis proceeds via (1) coalescence of endosomal vesicles delivering lumenal membrane and (2) docking of canalicular vesicles supplying translumenal flux, both of which are ERM-1–dependent processes (Khan et al., 2013). In support of this model, we here show that endosomal trafficking is indispensable for any lumen to form. Since IFs affect vesicular trafficking (Margiotta and Bucci, 2016), we asked if IFs might interact with ERM-1 in lumenogenesis by providing vesicle tracks. Unexpectedly, we found that IFs, conversely, restrict both endosomal and canalicular vesicle access to the lumen, a function that we show curbs lateral membrane expansion and cystogenesis, which in turn usurps the lumen's forward extension. We suggest that it is the triple IF lattice itself, transiently assembled into a perilumenal braid (Fig. 7 h), that spatially restrains, aligns, and centers the intracellular lumen. Such a function adds a novel,
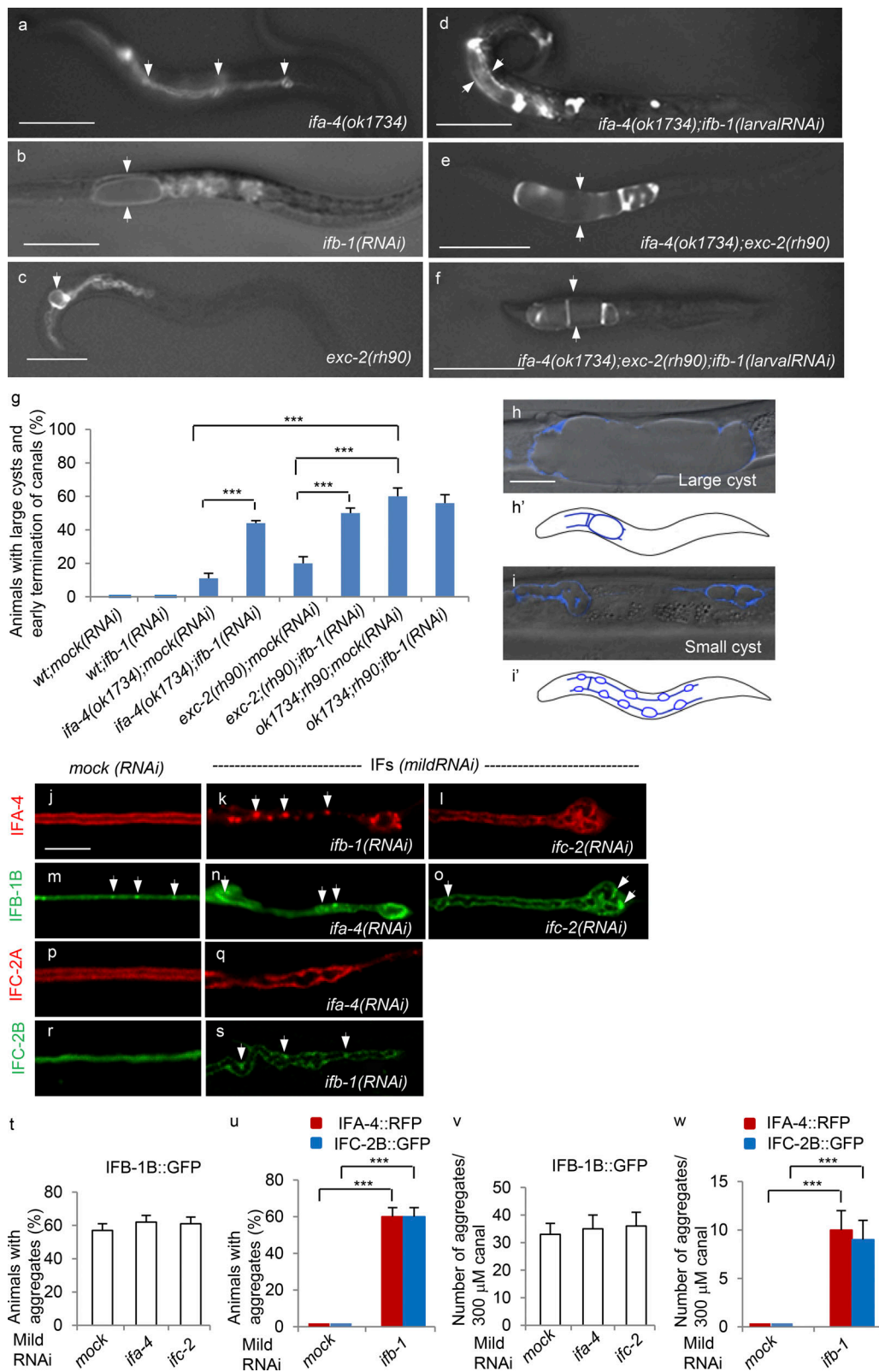
Figure 8. **IFA-4, IFB-1, and IFC-2 interact in excretory canal lumenogenesis.** See Fig. S4 for additional data. **(a–i)** Genetic interactions of the three canal IFs. **(a–h')** Epifluorescence/Nomarski overlays of P$_{sulp-5}$::GFP-labeled single and double IF mutant/(RNAi) canals. Note the multiple small cysts (a, arrows) along medium-length canals (compare i and i '), the large canal-cell-body–close cyst (b, arrows) without canal extension (compare h and h'), and the medium-sized cyst (c, arrow) and small cysts in short canals. All double mutant/RNAi animals have large cysts without lumen extension (d–f, h, and h'). Cyst size and canal length vary (see Materials and methods for quantification). **(g)** Quantification of genetic interactions. Note that all RNAi is conditionally induced at the L1 stage. **(h–i')** Prototypic canal/lumen phenotypes and corresponding schematics. **(j–s)** IFs are not required for their mutual recruitment to the lumen, but IFB-1

Khan et al.
A tensile endotube propels intracellular lumens

Journal of Cell Biology
https://doi.org/10.1083/jcb.201811175

2416

depletion induces aggregation of IFA-4 and IFC-2 at the lumen. Note the IFA-4::tagRFP and IFC-2::GFP aggregates (arrows, k and s) in IFB-1–depleted, but not IFC-2– and IFA-4–depleted, canals (l and q). IFB-1B aggregates are also present in WT canals (m–o). **(t–w)** Quantification of IF aggregates (see Materials and methods). Scale bars represent 100 μM (a–f) or 10 μM (in h for h and i and j for j–s).

IF-mediated control at the vesicle–lumen interface to the process of intracellular lumenogenesis, provides a new example for the emerging roles of cIFs as organizers of cytoplasmic space (Schwarz and Leube, 2016), and further supports a trafficking- and flux-based intracellular lumenogenesis model.

Because of its tensile properties (Kreplak et al., 2005, 2008; Kiss and Kellermayer, 2014), a perilumenal IF lattice can absorb intralumenal pressure. We also previously proposed that pulses of lateral water influx from varicosity-based aquaporin-rich canaliculi are converted into forward flux for canal lumen extension (Khan et al., 2013). In IF-depleted canals, lumens fail to expand between these lateral growth sites, supporting the idea, and suggesting that IFs effect this force conversion. Lumen diameter equilibration might, however, require more than canalicular vesicle spacing. In fact, AQP-8$^+$ canaliculi are only enriched in varicosities (Khan et al., 2013), and, upon IF depletion, exclusively cluster at varicosity cysts. Absorption of intralumenal pressure by the endotube should suffice to act as a lever for fluid-based force transduction, with no need to evoke active compressive forces. We therefore suggest that the tensile perilumenal cIF lattice converts concentric into forward flux at these lateral growth sites and perhaps also at lumen tips. The lattice's dynamic morphogenetic function in lumenogenesis thus also depends on its mechanical properties, extending the roles of cIFs in mechanotransduction to lumenal membranes (Jones et al., 2017; Sanghvi-Shah and Weber, 2017) and providing a first example of the ability of cIFs to transform an isotropic (fluid) into a directional force.

AFs are strictly required for lumen biogenesis, whereas IFs and MTs shape the lumen into forward extension
AFs, IFs, and MTs have been implicated in different aspects of intracellular lumenogenesis (Gervais and Casanova, 2010; Schottenfeld-Roames and Ghabrial, 2012; Kolotuev et al., 2013; Huber et al., 2015; Al-Hashimi et al., 2018), but their integration in this process, and thus a building plan for its construction, is missing. Our comparative and developmental analysis of AFs (via ACT-5/actin and its linker, ERM-1), IFs (via IFA-4, IFB-1, and IFC-2), and MTs (via TBB-2/tubulin) identified the antagonistic interactions of IFs with AFs and MTs in lumen expansion but synergistic interactions in lumen forward extension. We place these interactions to the vesicle–lumen interface: (1) ERM-1/AFs and MTs recruit endosomal and canalicular vesicles to the lumen, whereas IFs restrains their access (antagonism of IFs with AFs and MTs); (2) IFB-1 itself is recruited to the lumen by ERM-1 and TBB-2 (synergism of IFs with AFs and MTs). ERM-1/AFs, unlike IFs and MTs, initiate lumenogenesis via membrane biogenesis, whereas all three filaments are required for lumen forward extension, IFs indirectly (by restraining lateral growth) and MTs both directly (by providing vesicle tracks) and indirectly (by recruiting IFs). ERM-1/AFs thus expand the lumen, and MTs, like IFs, shape it into forward extension.

This analysis extends and supports specific roles of cytoskeletal molecules and their interaction in lumenogenesis in various tissues and species, suggesting the structural molecular basis of this process is conserved. IFs were previously proposed to interact with ERM-1 in lumen integrity and apical domain organization, but the nature of this interaction, although principally considered synergistic, is not clear (Haddad et al., 2002; Wald et al., 2005; Carberry et al., 2012; Gilbert et al., 2012). We identified the three cIFs as independent loss-of-function enhancers of ERM-1^{++} canal lumenogenesis, initially suggesting an antagonistic ERM-1/IF relationship (or no interaction; e.g., unspecific loss of cyst membrane resiliency). The subsequent analysis specified this relationship as more complex; ERM-1 indirectly recruits IFs to the lumen, which in turn restrain ERM-1's function in apical/lumenal domain expansion, with a net effect of lumen forward extension in this unicellular tube (we therefore interpret the ERM-1^{++} cyst enhancement by IF loss as a specific relief of this IF restraint and not as unspecific loss of membrane resiliency). In *Drosophila* terminal tracheal branches, AFs provide tracks to initiate intracellular lumenogenesis, and MTs move vesicles to the lumen (Gervais and Casanova, 2010; Schottenfeld-Roames and Ghabrial, 2012). Our study supports and specifies these findings and identifies the recruitment of perilumenal IFs as a second, novel, and apparently dominant MT function. This latter function has precedence in the ability of MTs to secure pancytoplasmic IF networks in flat epithelia and adds the unusual assembly of a concentric IF lattice to the intriguing but less well-appreciated structural roles of MTs in cellular morphogenesis (Kreitzer et al., 1999).

Collectively, the comparative analysis of three cytoskeletal filaments in capillary-like lumenogenesis provides an architectural plan for its intricate construction process, identifies new cytoskeletal requirements for lumen-directed vesicle trafficking, validates and specifies the ERM-1–IF interaction in apical/lumenal domain biogenesis and broadens it to unicellular tubes, and characterizes two independent (including one novel) structural functions of MTs in lumenogenesis.

The cytoskeletal architecture of an intracellular lumen
The comparative genetic and imaging analysis of three different cIFs furthermore permitted the characterization of their assembly as a perilumenal triple IF lattice. IFB-1 directly interacted with each IFA-4 and IFC-2 (e.g., during dimerization and/or polymerization), whereas IFA-4/IFB-1 and IFC-2/IFB-1 acted in parallel (e.g., during higher-order lattice assembly). Consistent with this construction plan, the loss of any IF disturbs, but loss of IFB-1 or of both IFA-4 and IFC-2 aborts, intracellular lumen extension. The three IFs encircle the lumen as superimposable lattices, with IFB-1 slightly closer to IFA-4 and IFC-2 than the latter to each other, implying that all IFs contribute to all lattice strands rather than intertwine (Fig. 10 a; a configuration distinct from a previously proposed, though not experimentally
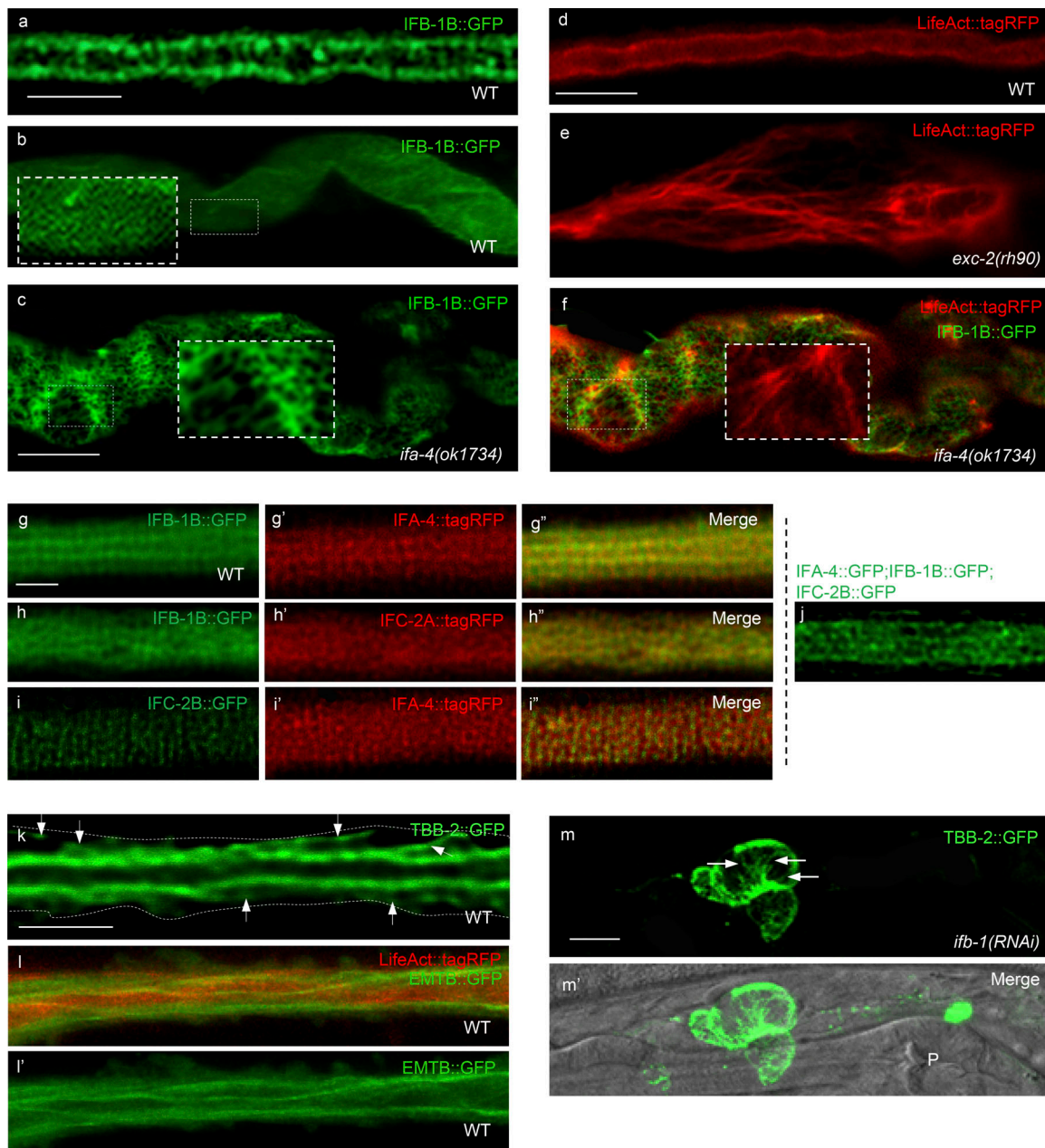
Figure 9. **IFB-1/IFA-4 and IFB-1/IFC-2 form a staggered perilumenal IF lattice, embedded between lumenal AFs and helical MTs.** The architecture of the trilayered submembranous canal lumen cytoskeletal contains distinct perilumenal IF (a–c and g–j), AF (d–f), and MT (k–m') assemblies. **(a–c)** IFB-1 forms a perilumenal lattice (b, inset) that remains intact, albeit distorted, around cysts (c, inset). **(d–f)** Perilumenal AFs form stress fiber–like strands around cysts (c and f, insets; compare distinct IF and AF assemblies [f is an overlay of c]). **(g–j)** The three IFs form parallel lattice strands, with overlapping IFB-1/IFA-4 (g–g") and IFB-1/IFC-2 (h–h") and staggered IFA-4/IFC-2 lattices (i–i"). The lattice strands do not interweave but combine to a superimposable triple lattice (j, canal lumen with three IF::GFP fusions; compare model in Fig. 10). **(k–m')** MTs form apical-to-basal tracks (k, arrows) and perilumenal helical strands (l and l') that are maintained around cysts (m and m'). The image is focused on the mid-lumen in k and the lumenal surface in l and l'. An anterior canal cyst is shown in m and m'. The image background is blackened in e, f, i–i", and m for clarity (see Fig. S6, 9E, 9F, 9I–I", and 9M, for corresponding originals). Scale bars represent 5 μM (in a for a and b and k for k–l'), 10 μM (c, in d for d–f, and m for m–m'), and 1 μM (in g for g–j).

endorsed, model; Al-Hashimi et al., 2018). The lattice widens around cysts, revealing its tensile properties. This tensile IF superstructure is consistent with the proposed dual IF function in spacing vesicles at the lumen and resisting hydrostatic pressure. We thus describe a novel higher-order circular assembly of three distinct perilumenal cIFs with a direct dynamic and biomechanical function in capillary-like intracellular lumenogenesis.

Intriguingly, this IF lattice rests on an actin endotube and is surrounded by helical strands of otherwise cytoplasmic MTs (a configuration also distinct from the model suggested in Al-Hashimi et al., 2018). MTs, versatile and resilient tubular filaments, have previously been reported to form circular arrangements in vertebrate cells (e.g., beneath the plasma membrane; Winckler and Solomon, 1991). Intriguingly, helical
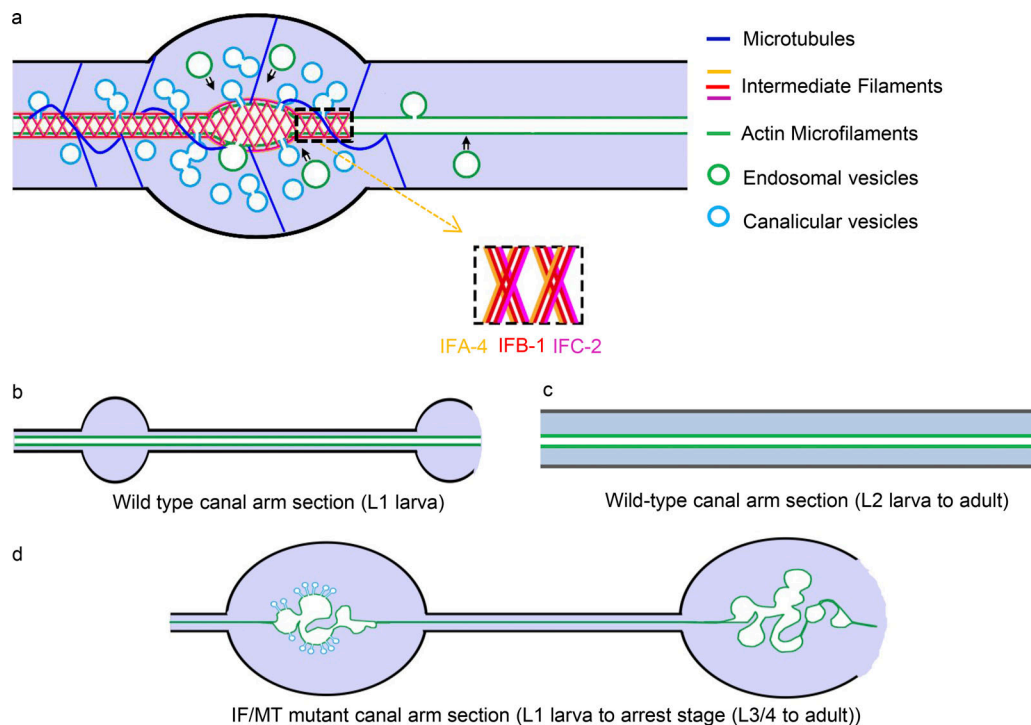
Figure 10. **Model for capillary-like intracellular lumenogenesis.** A tensile trilayered cytoskeletal endotube integrates the lateral addition of membrane and flux into forward extension. **(a)** Lateral growth site (varicosity; WT). A triple IF lattice, surrounded by helical MTs, spaces endosomal and canalicular vesicles along the AF-lined lumenal membrane, thereby integrating lateral into forward lumen extension (note that both the membrane and flux are added to the lateral side of the lumen). The same mechanism may operate during lumen tip extension (not shown). Apical/lumenal to basolateral MT strands are also indicated; additional cytoplasmic AFs and MTs are omitted for clarity. Inset shows assembly of IFs into a staggered lattice of IFB-1/IFA-4 and IFB-1/IFC-2 strands. **(b and c)** WT larval and adult canal arm section at lower magnification. Note that varicosities become integrated into canals during canal extension. The endomembrane compartment is omitted for clarity. **(d)** Tortuous multicystic varicosity phenotype in canals deprived of IFs or MTs during their extension phase. Note the excess lateral lumenal membrane and cyst formation in varicosities at the expense of intervaricosity lumen and canal development. Clusters of canalicular vesicles around cysts are indicated in the left varicosity, and endosomal vesicles are absent (consumed in cyst membranes).

MT strands promote axial growth in plants by inducing adjacent microfibrils to adopt shapes suited to transform isometric turgor pressure into directional growth (Lloyd and Chan, 2002). It is thus tempting to speculate that these MTs also shape the perilumenal IF assembly to transduce hydrostatic pressure during capillary-like lumenogenesis. Finally, the trilayered architecture of this cytoskeletal endotube may provide additional biophysical advantages, as suggested by material science's preference for tubing constructed from three layers of different materials, each with distinct mechanical properties (Hiroyuki et al., 2014).

Materials and methods

General
An online visual presentation of part of the methods described below is available in Zhang et al. (2017a) and Zhang et al. (2017b). The site includes videos demonstrating the mounting and immobilization techniques optimized for imaging the *C. elegans* excretory canal, as well as dissecting and confocal microscopy procedures and methods for quantifying excretory canal length and cyst size.

Nematode maintenance, strains, and classical genetics
WT (*C. elegans* variety Bristol, strain N2) and mutant worms were cultured and maintained and genetic crosses were performed using standard methods (Brenner, 1974). In general, worms were cultured on nematode growth medium (NGM) plates seeded with *Escherichia coli* OP50 (https://www.wormbase.org). Table S1 provides a list of the strains used in this study.

RNAi
RNAi screening was performed as outlined previously (Khan et al., 2013). Unless otherwise indicated, for single experiments, worms were fed bacterial clones harboring plasmids containing the DNA of a specific gene of interest, derived from the Ahringer genome-wide RNAi feeding library (Wellcome Trust/Cancer Research UK-Gurdon Institute, Cambridge, UK). Conditions to induce the bacterial polymerase to generate dsRNA on feeding plates were followed as described elsewhere (Timmons et al., 2001). In short, 2 mM IPTG and 25 µg/ml carbenicillin were added to the standard NMG media to make RNAi plates. RNAi plates were then dried at the bench for 2 d before use. Excess plates were stored at 4°C for no more than 2 mo. RNAi bacterial colonies were maintained on LB/ampicillin (50 µg/ml)/tetracycline (15 µg/ml) plates and usually restreaked on new plates every 15 d. To induce gene specific RNA depletion, RNAi bacteria containing the gene of interest were cultured in LB/ampicillin (50 µg/ml) broth for ≥6 h or overnight; 100 µl bacteria was removed and seeded on RNAi plates. The bacteria

were induced for ≥6 h on the IPTG-containing plates before adding the worms. Usually three or four L3 or L4 larvae were transferred to the plates containing the induced RNAi bacterial culture. After 2–4 d, F1 progeny, typically at the L1–L4 larval stage, were scored for canal phenotypes by dissecting or Nomarski microscopy (e.g., for short, long, thin, wide, and cystic canals; see below for quantification of canal phenotypes) or, if harboring fluorescent markers, by epifluorescence and/or confocal microscopy (see below, Imaging).

Mild RNAi was induced either by reducing the concentration of IPTG or by diluting the RNAi bacteria itself with empty vector bacteria as described previously (Zhang et al., 2017a). RNAi was conditionally induced at different stages of development by transferring eggs, L1, L2, L3, or L4 larvae (larval RNAi), or adult animals to RNAi plates and scoring the same generation (not their progeny, as in standard, parentally induced RNAi) over time. All experiments were repeated three or more times for each dataset.

Recombinant DNA procedures

Genes of interests were expressed in the excretory canal by cloning them between the canal specific *sulp-5* promoter at their 5′ ends and in frame with GFP or tagRFP marker genes at their 3′ ends using standard cloning procedures. Briefly, 1.2 kb of *sulp-5*'s upstream promoter was amplified by PCR from WT genomic DNA (see Table S2 for all primers used in this study). *ifa-4*, *ifb-1b*, *ifc-2a*, *ifc-2b*, and *tbb-2* cDNAs were PCR amplified from their respective cDNA plasmid clones (gifts from Y. Kohara, National Institute of Genetics, Mishima, Japan). GFP and tagRFP coding DNA fragments were PCR amplified from the plasmids ppD95.75 and pPD284, respectively (Fire et al., 1990; Addgene). The *sulp-5* promoter::cDNA::GFP::unc-54 3′UTR and the *sulp-5* promoter::cDNA::tagRFP::unc-54 3′ UTR chimeric DNAs were generated by using the PCR stitching method (Hobert, 2002). The *tbb-2* full-length genomic DNA with an ~1.9-kb upstream sequence was amplified by PCR using WT genomic DNA as template and then cloned into the GFP vector pPD95.75 between SphI and SmaI sites. All DNA ligations were performed using T4 ligase (Roche Diagnostics). The recombinant plasmid DNAs were transformed into *E. coli* XL1 Blue, and plasmid DNA was purified using a Miniprep kit (QIAGEN). All recombinant plasmids and PCR-stitching generated chimeric DNAs were sequenced to confirm their integrity. To generate transgenic lines, DNAs were injected into WT or mutant *C. elegans* gonads for germline transformation, with or without the *rol-6* marker DNA, using standard microinjection techniques (Stinchcomb et al., 1985; Mello et al., 1991).

Construction of transgenic lines overexpressing a fluorescent marker in the *C. elegans* excretory canal

The visual in vivo analysis of subcellular components of the *C. elegans* excretory canal is complicated by the typically low endogenous expression levels of its genes, mandating the introduction of more than one or two copies of fluorescently labeled transgenes. The overexpression of transgenes, on the other hand, tends to interfere with the development of the thin single-cell canal tube and its ultrathin lumenal endotube and can generate lumenal cysts or cytoplasmic vacuoles (Zhang et al., 2017b). To overexpress fluorescent fusion proteins in the canal (e.g., to generate ERM-1::GFP[++] and TBB-2::GFP[++] transgenic lines), the copy number of extrachromosomal transgenes was titrated by microinjecting a range of plasmid DNA concentrations (see above, Recombinant DNA procedures). Lines overexpressing the marker without inducing canal morphogenesis defects were selected. Overexpression was verified by either quantitative RT-PCR and/or ImageJ software (Khan et al., 2013; Zhang et al., 2017b; see below, ImageJ in the Quantification of endosomal vesicle number section).

Deletion mutants, crosses, and genotyping

Deletion mutants were extensively backcrossed with WT and the identity of all viable mutants with uncharacterized phenotypes was ascertained by genotyping during standard genetic crosses for labeling or to generate double mutants. For example, to generate the *ifa-4(ok1734); sulp-5p::gfp* strain, *ifa-4(ok1734)* hermaphrodites were mated to *sulp-5p::gfp* males and F1 GFP⁺ hermaphrodites isolated. F2 GFP⁺ hermaphrodites were cloned to single plates and allowed to lay eggs. Approximately 16 individual parents (F2) were subjected to PCR amplification using primers flanking the deletion. PCR DNA fragments were size separated by electrophoresis and visualized on agarose gels using standard techniques. Progeny of parents that only had the deletion-sized DNA fragment were selected and maintained as homozygous strain.

Mercury assay

A 200-mM stock solution of mercuric chloride ($HgCl_2$) was made. Dilutions were added either directly to the NGM media before pouring the plates or were added to the *E. coli* OP50 bacterial lawn on the NGM plate (plates were then air dried before use). Final mercury concentrations of 0.2 mM and 0.4 mM were used for the assays shown (concentrations >0.6 mM were determined to be lethal). Animals being analyzed were seeded onto the $HgCl_2$ supplemented feeding plates, and their F1 L4 larval progeny was scored for excretory canal phenotypes.

Aluminum chloride assay

1 ml of a 1.0-mM $AlCl_3$ stock solution was added to OP50 bacteria seeded onto NGM plates and spread homogeneously over the plate (concentrations >1.0 mM were determined to be lethal). As control, 1 ml sterile water was added in the same way. The plates were air dried, and several worms were immediately seeded onto the plates and placed at 20°C. F1 larvae were scored at the L4 stage for excretory canal phenotypes.

Imaging and confocal and dissecting microscopy

Bright-field and fluorescence dissecting micrographs were acquired using an Olympus SZX12 microscope, equipped with a custom-made high-power stereo fluorescent attachment (Kramer Scientific) and a digital CCD camera (Qimaging RETIGA 2000R) with Qcapture software. Live animals were directly imaged on plates. For differential interference contrast (Nomarski) and confocal microscopy, live animals were mounted on

glass slides. To avoid vacuolization in the canal cytoplasm or canal rupture, only a few animals were handpicked and anaesthetized in a drop of 5 µl 5% lidocaine solution and immediately processed (Zhang et al., 2017b). Nomarski and fluorescence micrographs were acquired using a Leica TCS SL laser-scanning confocal microscope and a Nikon Eclipse-Ti inverted microscope equipped with C2 confocal system. High-resolution confocal micrographs were acquired by a Zeiss LSM800 confocal microscope equipped with Airyscan superresolution capabilities using the high-resolution mode on single z-stacks.

To visualize the <2-µM-diameter canal tubes and their even smaller lumenal endotubes and subcellular components during embryonic and larval tubulogenesis, all confocal images were obtained with 60× or 100× objectives (see Khan et al. [2013]; and see Fig. S1 for stage-specific restrictions to the visual resolution of canal and canal lumens by confocal microscopy). Canals were spot checked for phenotypes along their lengths and assessed by parallel differential interference contrast/fluorescence imaging to determine diameter and length in comparison to body length and diameter (see below, Quantification of canal phenotypes). Exposure to fluorescent light was minimized to avoid bleaching, and images were obtained within minutes of mounting to avoid deformation of canal structures (Zhang et al., 2017b). Images were captured as single sections or a series of sections along the z axis with differing thicknesses (generally 0.1 to 1.0 µM). For multichannel images, individual channel intensity was adjusted and the samples were scanned sequentially to exclude the possibility of bleed-through between channels. Confocal imaging settings, such as pinhole size, LASER intensity, averaging, and other imaging parameters, were empirically determined based on fluorophore intensity and experimental setting. Deconvolution software was only used in Fig. 9, b (inset) and g–j (2 × 2D blind deconvolution; Nikon NIS elements), and images were not further edited except to adjust for brightness and contrast (Adobe Photoshop).

Fluorescence intensity measurement and quantification
For fluorescence intensity measurement each control and experimental set of images was acquired by identical imaging parameters (e.g., laser intensity; see above, Imaging). Fluorescence intensities in the acquired images were measured with NIS elements software (Fig. 7, i, j, m, and n; and Fig. S2, m and n). A line was drawn vertically across a canal arm, and a plot profile was generated by the software. Intensity was shown as gray value on the y axis in each graphical plot (Fig. 7, i′, j′, m′, and n′; and Fig. S2, m′ and n′). Gray values of three or more images were used for statistical analysis (Fig. 7, k and o; and Fig. S2 o).

Quantification of canal phenotypes
Unless otherwise indicated, posterior canal arm length and cyst size were measured in comparison with body length and diameter. Canal length was scored as 0, 1/4, 1/2, 3/4, and 1; 0 indicates no posterior extension of the canal from the point of canal bifurcation at the height of the pharynx, and 1 indicates full-length canal extension up to the tip of the tail, or up to the expected length of the developmental stage (as indicated). Cyst size was scored as small (less than one third of body diameter)

and large (more than one third of body diameter). For details, see Zhang et al. (2017b).

Quantification of endosomal vesicle number and sizes in the excretory canal
The number of fluorescently labeled endosomes in controls and different transgenic lines was compared in same-stage animals grown under the same culture conditions and counted from confocal images acquired using identical imaging settings (see above, Imaging). The total number of vesicles in a 100-µM length of a canal arm was counted manually (visually) and assessed in different parts along the lengths of canals. For each data point, five or more animals were counted. To integrate the distinct parameters of mutant/RNAi endosomes (size, shape, and aggregation) for comparison, we developed a size-quantification method using ImageJ (see above, Fluorescence intensity measurement). Vesicles and vesicle aggregates were measured from confocal images by drawing a line vertically, diagonally, or horizontally (depending on the orientation of the vesicle) across the largest diameter of a given vesicle in a 2D setting. A plot profile was generated by the software. The fluorescence intensity of the vesicle was shown as gray value on the y axis, and the diameter of the vesicle was shown as distance (pixels) on the x axis on the graphical plot (see Fig. S3, o–r). The size of each vesicle was expressed in pixels and determined manually from each plot. The sizes of 10 random vesicles were determined from one image while visually moving along a posterior canal arm, and ≥30 vesicles in total from three or more images were used to calculate the mean diameter of a vesicle and for statistical analysis.

Quantification of IF aggregates in the excretory canal
To compare the number of IF aggregates in IF mutant/RNAi transgenic lines harboring different fluorescently labeled IF fusions, we acquired confocal microscopic images of posterior canal arms of same-stage animals grown under identical culture conditions and analyzed with identical imaging settings (lowest intensity laser settings were used to avoid the introduction of artifacts; see above, Imaging). IFA-4::GFP, IFB-1::GFP, IFC-2B::GFP, and IFC-2A::GFP or IFA-4::RFP, IFB-1::RFP, IFC-2B::RFP, and IFC-2A::RFP puncta were counted manually. The percentage of animals with aggregates per total number of animals was assessed, and the number of puncta in a 300-µM stretch of a posterior canal arm per animal was counted. More than 50 animals were analyzed to calculate the percentage of animals with puncta, and ≥10 animals were used for calculating the mean number of puncta in 300 µM of a canal arm and for statistical analysis.

TEM
Under a dissecting microscope, *C. elegans* cuticles were "nicked" with a razor blade in a drop of fixative (2.5% glutaraldehyde and 1.0% paraformaldehyde in 0.05 M sodium cacodylate buffer, pH 7.4, plus 3.0% sucrose) in order to allow fixative to penetrate the somewhat impermeable cuticle. After an initial 2-h fixation at room temperature, the specimens were transferred into fresh fixative and stored overnight at 4°C. Specimens were rinsed

several times in 0.1 M cacodylate buffer and then postfixed in 1.0% osmium tetroxide in 0.1 M cacodylate buffer for 2 h on ice. Specimens were rinsed several times in 0.1 M cacodylate buffer and then embedded in 2.0% agarose in PBS for ease of handling. The agarose blocks were dehydrated through a graded series of increasing concentrations of ethanol up to 100% and then exchanged with 100% propylene oxide and preinfiltrated overnight on a rocker in a 1:1 mixture of propylene oxide/Eponate resin (Ted Pella). The following day, the agarose blocks were infiltrated in 100% Eponate resin for several hours and subsequently embedded in flat molds in fresh Eponate resin and allowed to polymerize a minimum of 24 h at 60°C. Thin sections were cut on a Leica UC7 ultramicrotome and collected on formvar-coated grids, poststained with uranyl acetate and Reynold's lead citrate, and viewed in a JEOL 1011 TEM at 80 kV equipped with an AMT digital imaging system (Advanced Microscopy Techniques).

Statistics

For statistical analyses, we used the Microsoft Excel program. All values are mean ± SD from three or more experimental datasets. P values were calculated using the two-tailed t test. The number of independent experiments (n) is indicated in the text and figure legends, and sample sizes (N) are indicated where necessary. *, $P < 0.05$; **, $P < 0.001$; ***, $P < 0.0001$.

Online supplemental material

Fig. S1 shows that three cIFs are required for intracellular lumenogenesis in the *C. elegans* excretory canal and interact with ERM-1 in this process. Fig. S2 shows gene structures, developmental expression patterns, and subcellular localization of IFA-4, IFB-1, and IFC-2 and isoforms, as well as the functional IF requirement for canal development versus canal maintenance. Fig. S3 shows comparative analysis of the functions of IFs, AFs, and MTs in canal morphogenesis. Fig. S4 shows displacement of canalicular vesicles in *tbb*-2–depleted canals; genetic interactions among the three IFs with regard to overall viability; and pharmacological interference with IFs by $AlCl_3$. Fig. S5 shows corresponding uncropped original images for Figs. 2 and 3. Fig. S6 shows corresponding uncropped original images for Figs. 7 and 9. Table S1 lists strains used in this study. Table S2 lists PCR primers used in this study.

References

Al-Hashimi, H., D.H. Hall, B.D. Ackley, E.A. Lundquist, and M. Buechner. 2018. Tubular Excretory Canal Structure Depends on Intermediate Filaments EXC-2 and IFA-4 in *Caenorhabditis elegans*. *Genetics*. 210: 637–652.

Armenti, S.T., E. Chan, and J. Nance. 2014. Polarized exocyst-mediated vesicle fusion directs intracellular lumenogenesis within the *C. elegans* excretory cell. *Dev. Biol.* 394:110–121. https://doi.org/10.1016/j.ydbio.2014.07.019

Bär, T., F.H. Güldner, and J.R. Wolff. 1984. "Seamless" endothelial cells of blood capillaries. *Cell Tissue Res.* 235:99–106. https://doi.org/10.1007/BF00213729

Block, J., V. Schroeder, P. Pawelzyk, N. Willenbacher, and S. Köster. 2015. Physical properties of cytoplasmic intermediate filaments. *Biochim. Biophys. Acta.* 1853(11, 11 Pt B):3053–3064. https://doi.org/10.1016/j.bbamcr.2015.05.009

Brenner, S. 1974. The genetics of *Caenorhabditis elegans*. *Genetics*. 77:71–94.

Buechner, M. 2002. Tubes and the single *C. elegans* excretory cell. *Trends Cell Biol.* 12:479–484. https://doi.org/10.1016/S0962-8924(02)02364-4

Buechner, M., D.H. Hall, H. Bhatt, and E.M. Hedgecock. 1999. Cystic canal mutants in *Caenorhabditis elegans* are defective in the apical membrane domain of the renal (excretory) cell. *Dev. Biol.* 214:227–241. https://doi.org/10.1006/dbio.1999.9398

Carberry, K., T. Wiesenfahrt, F. Geisler, S. Stöcker, H. Gerhardus, D. Überbach, W. Davis, E. Jorgensen, R.E. Leube, and O. Bossinger. 2012. The novel intestinal filament organizer IFO-1 contributes to epithelial integrity in concert with ERM-1 and DLG-1. *Development*. 139:1851–1862. https://doi.org/10.1242/dev.075788

Carmeliet, P. 2003. Angiogenesis in health and disease. *Nat. Med.* 9:653–660. https://doi.org/10.1038/nm0603-653

Chang, L., and R.D. Goldman. 2004. Intermediate filaments mediate cytoskeletal crosstalk. *Nat. Rev. Mol. Cell Biol.* 5:601–613. https://doi.org/10.1038/nrm1438

Coch, R.A., and R.E. Leube. 2016. Intermediate Filaments and Polarization in the Intestinal Epithelium. *Cells*. 5:5. https://doi.org/10.3390/cells5030032

Etienne-Manneville, S. 2018. Cytoplasmic Intermediate Filaments in Cell Biology. *Annu. Rev. Cell Dev. Biol.* 34:1–28. https://doi.org/10.1146/annurev-cellbio-100617-062534

Fire, A., S.W. Harrison, and D. Dixon. 1990. A modular set of lacZ fusion vectors for studying gene expression in *Caenorhabditis elegans*. *Gene*. 93:189–198. https://doi.org/10.1016/0378-1119(90)90224-F

Folkman, J., and C. Haudenschild. 1980. Angiogenesis in vitro. *Nature*. 288:551–556. https://doi.org/10.1038/288551a0

Khan et al.
A tensile endotube propels intracellular lumens

Journal of Cell Biology 2422
https://doi.org/10.1083/jcb.201811175

Fuchs, E. 1995. Keratins and the skin. *Annu. Rev. Cell Dev. Biol.* 11:123–153. https://doi.org/10.1146/annurev.cb.11.110195.001011

Fujita, M., D. Hawkinson, K.V. King, D.H. Hall, H. Sakamoto, and M. Buechner. 2003. The role of the ELAV homologue EXC-7 in the development of the *Caenorhabditis elegans* excretory canals. *Dev. Biol.* 256: 290–301. https://doi.org/10.1016/S0012-1606(03)00040-X

Gebala, V., R. Collins, I. Geudens, L.K. Phng, and H. Gerhardt. 2016. Blood flow drives lumen formation by inverse membrane blebbing during angiogenesis in vivo. *Nat. Cell Biol.* 18:443–450. https://doi.org/10.1038/ncb3320

Gervais, L., and J. Casanova. 2010. In vivo coupling of cell elongation and lumen formation in a single cell. *Curr. Biol.* 20:359–366. https://doi.org/10.1016/j.cub.2009.12.043

Gilbert, S., A. Loranger, J.N. Lavoie, and N. Marceau. 2012. Cytoskeleton keratin regulation of FasR signaling through modulation of actin/ezrin interplay at lipid rafts in hepatocytes. *Apoptosis.* 17:880–894. https://doi.org/10.1007/s10495-012-0733-2

Haddad, L.A., N. Smith, M. Bowser, Y. Niida, V. Murthy, C. Gonzalez-Agosti, and V. Ramesh. 2002. The TSC1 tumor suppressor hamartin interacts with neurofilament-L and possibly functions as a novel integrator of the neuronal cytoskeleton. *J. Biol. Chem.* 277:44180–44186. https://doi.org/10.1074/jbc.M207211200

Hahn-Windgassen, A., and M.R. Van Gilst. 2009. The *Caenorhabditis elegans* HNF4alpha Homolog, NHR-31, mediates excretory tube growth and function through coordinate regulation of the vacuolar ATPase. *PLoS Genet.* 5:e1000553. https://doi.org/10.1371/journal.pgen.1000553

Herrmann, H., H. Bär, L. Kreplak, S.V. Strelkov, and U. Aebi. 2007. Intermediate filaments: from cell architecture to nanomechanics. *Nat. Rev. Mol. Cell Biol.* 8:562–573. https://doi.org/10.1038/nrm2197

Herwig, L., Y. Blum, A. Krudewig, E. Ellertsdottir, A. Lenard, H.G. Belting, and M. Affolter. 2011. Distinct cellular mechanisms of blood vessel fusion in the zebrafish embryo. *Curr. Biol.* 21:1942–1948. https://doi.org/10.1016/j.cub.2011.10.016

Hiroyuki, S., S. Motohiro, and P. Sung-Jin. 2014. Suppression of brazier effect in multilayered cylinders. *Adv. Condens. Matter Phys.* 2014:923896.

Hobert, O. 2002. PCR fusion-based approach to create reporter gene constructs for expression analysis in transgenic *C. elegans*. *Biotechniques.* 32: 728–730. https://doi.org/10.2144/02324bm01

Hogan, B.L., and P.A. Kolodziej. 2002. Organogenesis: molecular mechanisms of tubulogenesis. *Nat. Rev. Genet.* 3:513–523. https://doi.org/10.1038/nrg840

Huber, F., A. Boire, M.P. López, and G.H. Koenderink. 2015. Cytoskeletal crosstalk: when three different personalities team up. *Curr. Opin. Cell Biol.* 32:39–47. https://doi.org/10.1016/j.ceb.2014.10.005

Hüsken, K., T. Wiesenfahrt, C. Abraham, R. Windoffer, O. Bossinger, and R.E. Leube. 2008. Maintenance of the intestinal tube in Caenorhabditis elegans: the role of the intermediate filament protein IFC-2. *Differentiation.* 76:881–896. https://doi.org/10.1111/j.1432-0436.2008.00264.x

Iwatsuki, H., and M. Suda. 2010. Seven kinds of intermediate filament networks in the cytoplasm of polarized cells: structure and function. *Acta Histochem. Cytochem.* 43:19–31. https://doi.org/10.1267/ahc.10009

Jones, J.C., C.Y. Kam, R.M. Harmon, A.V. Woychek, S.B. Hopkinson, and K.J. Green. 2017. Intermediate Filaments and the Plasma Membrane. *Cold Spring Harb. Perspect. Biol.* 9:9. https://doi.org/10.1101/cshperspect.a025866

Kamei, M., W.B. Saunders, K.J. Bayless, L. Dye, G.E. Davis, and B.M. Weinstein. 2006. Endothelial tubes assemble from intracellular vacuoles in vivo. *Nature.* 442:453–456. https://doi.org/10.1038/nature04923

Karabinos, A., H. Schmidt, J. Harborth, R. Schnabel, and K. Weber. 2001. Essential roles for four cytoplasmic intermediate filament proteins in *Caenorhabditis elegans* development. *Proc. Natl. Acad. Sci. USA.* 98: 7863–7868. https://doi.org/10.1073/pnas.121169998

Karabinos, A., E. Schulze, J. Schünemann, D.A. Parry, and K. Weber. 2003. In vivo and in vitro evidence that the four essential intermediate filament (IF) proteins A1, A2, A3 and B1 of the nematode *Caenorhabditis elegans* form an obligate heteropolymeric IF system. *J. Mol. Biol.* 333:307–319. https://doi.org/10.1016/j.jmb.2003.08.041

Khan, L.A., H. Zhang, N. Abraham, L. Sun, J.T. Fleming, M. Buechner, D.H. Hall, and V. Gobel. 2013. Intracellular lumen extension requires ERM-1-dependent apical membrane expansion and AQP-8-mediated flux. *Nat. Cell Biol.* 15:143–156. https://doi.org/10.1038/ncb2656

Kiss, B., and M.S. Kellermayer. 2014. Stretching desmin filaments with receding meniscus reveals large axial tensile strength. *J. Struct. Biol.* 186: 472–480. https://doi.org/10.1016/j.jsb.2014.04.004

Kochhan, E., A. Lenard, E. Ellertsdottir, L. Herwig, M. Affolter, H.G. Belting, and A.F. Siekmann. 2013. Blood flow changes coincide with cellular rearrangements during blood vessel pruning in zebrafish embryos. *PLoS One.* 8:e75060. https://doi.org/10.1371/journal.pone.0075060

Kolotuev, I., V. Hyenne, Y. Schwab, D. Rodriguez, and M. Labouesse. 2013. A pathway for unicellular tube extension depending on the lymphatic vessel determinant Prox1 and on osmoregulation. *Nat. Cell Biol.* 15: 157–168. https://doi.org/10.1038/ncb2662

Kreitzer, G., G. Liao, and G.G. Gundersen. 1999. Detyrosination of tubulin regulates the interaction of intermediate filaments with microtubules in vivo via a kinesin-dependent mechanism. *Mol. Biol. Cell.* 10:1105–1118. https://doi.org/10.1091/mbc.10.4.1105

Kreplak, L., H. Bär, J.F. Leterrier, H. Herrmann, and U. Aebi. 2005. Exploring the mechanical behavior of single intermediate filaments. *J. Mol. Biol.* 354:569–577. https://doi.org/10.1016/j.jmb.2005.09.092

Kreplak, L., H. Herrmann, and U. Aebi. 2008. Tensile properties of single desmin intermediate filaments. *Biophys. J.* 94:2790–2799. https://doi.org/10.1529/biophysj.107.119826

Kushkuley, J., S. Metkar, W.K. Chan, S. Lee, and T.B. Shea. 2010. Aluminum induces neurofilament aggregation by stabilizing cross-bridging of phosphorylated c-terminal sidearms. *Brain Res.* 1322:118–123. https://doi.org/10.1016/j.brainres.2010.01.075

Lant, B., B. Yu, M. Goudreault, D. Holmyard, J.D. Knight, P. Xu, L. Zhao, K. Chin, E. Wallace, M. Zhen, et al. 2015. CCM-3/STRIPAK promotes seamless tube extension through endocytic recycling. *Nat. Commun.* 6: 6449. https://doi.org/10.1038/ncomms7449

Lloyd, C., and J. Chan. 2002. Helical microtubule arrays and spiral growth. *Plant Cell.* 14:2319–2324. https://doi.org/10.1105/tpc.141030

Lubarsky, B., and M.A. Krasnow. 2003. Tube morphogenesis: making and shaping biological tubes. *Cell.* 112:19–28. https://doi.org/10.1016/S0092-8674(02)01283-7

Margiotta, A., and C. Bucci. 2016. Role of Intermediate Filaments in Vesicular Traffic. *Cells.* 5:5. https://doi.org/10.3390/cells5020020

Mattingly, B.C., and M. Buechner. 2011. The FGD homologue EXC-5 regulates apical trafficking in C. elegans tubules. *Dev. Biol.* 359:59–72. https://doi.org/10.1016/j.ydbio.2011.08.011

Mello, C.C., J.M. Kramer, D. Stinchcomb, and V. Ambros. 1991. Efficient gene transfer in C.elegans: extrachromosomal maintenance and integration of transforming sequences. *EMBO J.* 10:3959–3970. https://doi.org/10.1002/j.1460-2075.1991.tb04966.x

Nelson, F.K., and D.L. Riddle. 1984. Functional study of the *Caenorhabditis elegans* secretory-excretory system using laser microsurgery. *J. Exp. Zool.* 231:45–56. https://doi.org/10.1002/jez.1402310107

Omary, M.B. 2009. "IF-pathies": a broad spectrum of intermediate filament-associated diseases. *J. Clin. Invest.* 119:1756–1762. https://doi.org/10.1172/JCI39894

Omary, M.B., P.A. Coulombe, and W.H. McLean. 2004. Intermediate filament proteins and their associated diseases. *N. Engl. J. Med.* 351:2087–2100. https://doi.org/10.1056/NEJMra040319

Oriolo, A.S., F.A. Wald, V.P. Ramsauer, and P.J. Salas. 2007. Intermediate filaments: a role in epithelial polarity. *Exp. Cell Res.* 313:2255–2264. https://doi.org/10.1016/j.yexcr.2007.02.030

Rao, M.V., P.S. Mohan, A. Kumar, A. Yuan, L. Montagna, J. Campbell, E.M. Veeranna, E.M. Espreafico, J.P. Julien, and R.A. Nixon. 2011. The myosin Va head domain binds to the neurofilament-L rod and modulates endoplasmic reticulum (ER) content and distribution within axons. *PLoS One.* 6:e17087. https://doi.org/10.1371/journal.pone.0017087

Richardson, C.E., K.A. Spilker, J.G. Cueva, J. Perrino, M.B. Goodman, and K. Shen. 2014. PTRN-1, a microtubule minus end-binding CAMSAP homolog, promotes microtubule function in *Caenorhabditis elegans* neurons. *eLife.* 3:e01498. https://doi.org/10.7554/eLife.01498

Sanghvi-Shah, R., and G.F. Weber. 2017. Intermediate Filaments at the Junction of Mechanotransduction, Migration, and Development. *Front. Cell Dev. Biol.* 5:81. https://doi.org/10.3389/fcell.2017.00081

Schottenfeld-Roames, J., and A.S. Ghabrial. 2012. Whacked and Rab35 polarize dynein-motor-complex-dependent seamless tube growth. *Nat. Cell Biol.* 14:386–393. https://doi.org/10.1038/ncb2454

Schwarz, N., and R.E. Leube. 2016. Intermediate Filaments as Organizers of Cellular Space: How They Affect Mitochondrial Structure and Function. *Cells.* 5:5. https://doi.org/10.3390/cells5030030

Shaye, D.D., and I. Greenwald. 2015. The disease-associated formin INF2/EXC-6 organizes lumen and cell outgrowth during tubulogenesis by regulating F-actin and microtubule cytoskeletons. *Dev. Cell.* 32:743–755. https://doi.org/10.1016/j.devcel.2015.01.009

Khan et al.
A tensile endotube propels intracellular lumens

Sigurbjörnsdóttir, S., R. Mathew, and M. Leptin. 2014. Molecular mechanisms of de novo lumen formation. *Nat. Rev. Mol. Cell Biol.* 15:665–676. https://doi.org/10.1038/nrm3871

Song, Y., M. Eng, and A.S. Ghabrial. 2013. Focal defects in single-celled tubes mutant for Cerebral cavernous malformation 3, GCKIII, or NSF2. *Dev. Cell.* 25:507–519. https://doi.org/10.1016/j.devcel.2013.05.002

Stinchcomb, D.T., J.E. Shaw, S.H. Carr, and D. Hirsh. 1985. Extrachromosomal DNA transformation of *Caenorhabditis elegans. Mol. Cell. Biol.* 5: 3484–3496. https://doi.org/10.1128/MCB.5.12.3484

Sundaram, M.V., and M. Buechner. 2016. The *Caenorhabditis elegans* Excretory System: A Model for Tubulogenesis, Cell Fate Specification, and Plasticity. *Genetics.* 203:35–63. https://doi.org/10.1534/genetics.116.189357

Sundaram, M.V., and J.D. Cohen. 2017. Time to make the doughnuts: Building and shaping seamless tubes. *Semin. Cell Dev. Biol.* 67:123–131. https://doi.org/10.1016/j.semcdb.2016.05.006

Timmons, L., D.L. Court, and A. Fire. 2001. Ingestion of bacterially expressed dsRNAs can produce specific and potent genetic interference in *Caenorhabditis elegans. Gene.* 263:103–112. https://doi.org/10.1016/S0378-1119(00)00579-5

Wald, F.A., A.S. Oriolo, M.L. Casanova, and P.J. Salas. 2005. Intermediate filaments interact with dormant ezrin in intestinal epithelial cells. *Mol. Biol. Cell.* 16:4096–4107. https://doi.org/10.1091/mbc.e05-03-0242

Winckler, B., and F. Solomon. 1991. A role for microtubule bundles in the morphogenesis of chicken erythrocytes. *Proc. Natl. Acad. Sci. USA.* 88: 6033–6037. https://doi.org/10.1073/pnas.88.14.6033

Woo, W.M., A. Goncharov, Y. Jin, and A.D. Chisholm. 2004. Intermediate filaments are required for C. elegans epidermal elongation. *Dev. Biol.* 267:216–229. https://doi.org/10.1016/j.ydbio.2003.11.007

Zhang, H., F. Landmann, H. Zahreddine, D. Rodriguez, M. Koch, and M. Labouesse. 2011. A tension-induced mechanotransduction pathway promotes epithelial morphogenesis. *Nature.* 471:99–103. https://doi.org/10.1038/nature09765

Zhang, N., L.A. Khan, E. Membreno, G. Jafari, S. Yan, H. Zhang, and V. Gobel. 2017a. The C. elegans Intestine As a Model for Intercellular Lumen Morphogenesis and In Vivo Polarized Membrane Biogenesis at the Single-cell Level: Labeling by Antibody Staining, RNAi Loss-of-function Analysis and Imaging. *J. Vis. Exp.* https://doi.org/10.3791/56100

Zhang, N., E. Membreno, S. Raj, H. Zhang, L.A. Khan, and V. Gobel. 2017b. The C. elegans Excretory Canal as a Model for Intracellular Lumen Morphogenesis and In Vivo Polarized Membrane Biogenesis in a Single Cell: labeling by GFP-fusions, RNAi Interaction Screen and Imaging. *J. Vis. Exp.* https://doi.org/10.3791/56101